ARASHI
SCIENTIFIC PUBLISHERS

Arashi Journal of Metals & Material Sciences
Volume 3, Issue 1 (Jan–Dec) 2026, pp. 61–83
DOI: 10.54646/jmms.2026.0007
www.asp-jmms.com

Extended Review

Metal sulfide derived photocatalyst for wastewater treatment

Vivaan Anand[1], Abhineet Singh[2], Naveen Thakur[2], Anchal Panwar[2], Simran Sharma[2], Akshay Chawla[2] and Sonu[2]*

[1]Woodstock School, Mussoorie, Uttarakhand
[2]School of Advanced Chemical Sciences, Shoolini University, Solan, India

***Correspondence:**
Sonu,
sonuchem.12@gmail.com

Received: 01 September 2026; **Accepted:** 22 September 2026; **Published:** 04 October 2026

சுருக்கம்:
சுற்றுச்சூழல் மாசுபாடு உலகெங்கும் உள்ள சூழல் மண்டலங்களுக்கு அச்சுறுத்தலாக விளங்கும் ஒரு தீவிரப் பிரச்சினையாகும். சுற்றுச்சூழலை மீட்டெடுப்பதற்கான பல முறைகள் உருவாக்கப்பட்டுள்ளன. உலோக சல்பைடு அடிப்படையிலான குறைக்கடத்தி ஒளி வினையூக்கம், அதன் சாதகமான பேண்ட்கேப் அமைப்புகள், சிறந்த ஒளி உறிஞ்சும் திறன் மற்றும் மிகுந்த வினையூக்கச் செயல்பாடு ஆகியவற்றின் காரணமாக ஒரு சாத்தியமான தீர்வாகப் பரிந்துரைக்கப்பட்டுள்ளது. எங்கள் ஆய்வில், சுற்றுச்சூழல் சீரமைப்புத் துறையில் பயன்படுத்தப்படும் உலோக சல்பைடு அடிப்படையிலான ஒளி வினையூக்கிகளின் தற்போதைய முன்னேற்றங்கள் விரிவாக விவாதிக்கப்பட்டுள்ளன. உலோக சல்பைடு குறைக்கடத்திகளின் அடிப்படைக் கருத்துகளும் தனித்துவமான நன்மைகளும் ஆழமாக ஆராயப்பட்டுள்ளன. விரைவான மின்னூட்ட மறுஇணைவு, ஒளி அரிப்பு போன்ற உள்ளார்ந்த வரம்புகளைச் சமாளிக்க, ஊக்கமருந்தேற்றம், ஹெட்டரோ சந்திப்புகளை உருவாக்குதல், காலி இடப் பொறியியல் போன்ற பல்வேறு தொகுப்பு மற்றும் மாற்றியமைப்பு அணுகுமுறைகள் குறிப்பிடப்பட்டுள்ளன. ஒளி அரிப்பின் வழிமுறைகள், அதனைத் தணிக்கும் உத்திகளான தியாக முகவர்கள் மற்றும் ஹெட்டரோ கட்டமைப்பு உருவாக்கம் ஆகியவற்றுக்குச் சிறப்புக் கவனம் அளிக்கப்பட்டுள்ளது. இலட்சிய மாதிரி அமைப்புகளுக்கு அப்பால், உண்மையான கழிவுநீர் தளங்கள் ஒளி வினையூக்கச் செயல்திறனில் ஏற்படுத்தும் தாக்கத்தை, குறிப்பாக நைட்ரேட்டுகள், சல்பேட்டுகள், குளோரைடுகள் போன்ற உடன்வாழ் கனிம அயனிகளின் தாக்கத்தை, இக்கட்டுரை மதிப்பாய்வு செய்து விமர்சன ரீதியாக விவாதிக்கிறது. இறுதியாக, இத்துறையின் தற்போதைய தொழில்நுட்பச் சிரமங்கள், கட்டுப்பாடுகள் மற்றும் எதிர்காலச் சாத்தியக்கூறுகள் வலியுறுத்தப்பட்டுள்ளன. சுற்றுச்சூழலுக்கு நிலைத்த சீரமைப்பிற்கான உயர்திறன் உலோக சல்பைடு ஒளி வினையூக்கிகளை உருவாக்குவதற்கான அடிப்படை கட்டமைப்பும் உத்தி சார்ந்த அணுகுமுறையும் இக்கட்டுரையில் முன்வைக்கப்பட்டுள்ளன.

Abstract:
Pollution in the environment is a serious problem that threatens the ecosystems all over the world, and methods to restore the environment have been developed. Metal sulfide-derived semiconductor (SC) photocatalysis has been suggested as a possible method because of its favorable bandgap configurations, remarkable light-harvesting activity, and excellent catalytic activity. In our work, current progresses of metal sulfide-derived photocatalysts applied to the field of environmental remediation are comprehensively discussed. The basic ideas and unique benefits of metal sulfide SC s are thoroughly examined. Various approaches to synthesis and modification, such as doping, formation of heterojunctions, and vacancy engineering, are mentioned to counteract the intrinsic limitations like fast charge recombination and photocorrosion. Special consideration is given to mechanisms of photocorrosion and mitigation techniques like sacrificial agents and heterostructure fabrication. In addition to idealized model systems, the paper reviews and critically discusses the impact of the real wastewater matrices on photocatalytic performance, particularly the influence of coexisting inorganic ions, such as nitrates, sulfates, and chlorides. Lastly, the field's present technical difficulties, constraints, and potential are emphasized. A basic framework and strategic approach for the development of high-performance metal sulfide photocatalysts meant for environmentally sustainable remediation are presented in this paper.

Keywords: Metal sulfide photocatalysts, Photocatalysis, Wastewater treatment, Environmental remediation, Heterojunction engineering

CC BY

ISSN: 3107-3581 (online)

Introduction

Growing industrialization, growth, and urbanization raised serious environmental issues (1, 2). Due to poor management and insufficient treatment of wastewater before it is released into the environment, a large number of sources, especially industrial waste, are the main contaminant of our aquatic ecosystem. Poisonous dyes, antibiotics, insecticides, and toxic compounds from a variety of industries, including dyeing, printmaking, polymers, textiles, agriculture, and nuclear waste, make up the substantial amount of contaminated industrial effluent that endangers clean water and poses a serious risk to aquatic ecosystems and human health. The prevalence of air pollutants such as volatile organic compounds (VOCs), toxic gases, and pathogens in both outdoor and indoor environments has become a global concern issue. Currently, various sectors, including the Environmental Protection Agency (EPA) and the World Health Organization (WHO), have urged manufacturers worldwide to refrain from discharging contaminated water. Consequently, numerous international buyers have canceled orders from industries lacking internationally standardized wastewater treatment facilities. Additionally, significant research is focused on creating solutions that can potentially resolve these challenges both technically and economically (2). These include adsorption (3, 4), precipitation (5), biodegradation (6, 7), solvent extraction (8, 9), membrane separation (10, 11), chlorination (12, 13), ozonation (14, 15), ion exchange (16), and sono-degradation (17, 18). Although, there are multiple adverse effects of these approaches, such as high operating costs, scalability restrictions, hazardous byproducts, and comparatively poor rates of elimination and secondary waste management. Advanced oxidation processes (AOPs), such as sulfate radical-based oxidation (19), electrolysis (20), and photocatalysis (21), have been extensively utilized in comparison to standard wastewater treatment methods. Whereas photocatalytic degradation of certain pollutants with solar energy has several benefits, including environmental sustainability, cost-effectiveness, high efficiency, and eco-friendly attributes.

Photocatalysis promotes pollutant decomposition using light-activated, semiconductor (SC)-mediated AOPs (22, 23). Electrons (e^-s) are induced from the valence band (VB) to the conduction band (CB) when the SC photocatalyst is exposed to light energy higher than or equal to its bandgap (Eg), leaving holes (h^+) in the VB. After migrating to the catalyst surface, these photogenerated charge carriers (e^-–h^+) underwent significant redox reactions (reduction/oxidation reaction) with ambient oxygen molecules (O_2) and adsorbed water (H_2O), resulting in the production of highly reactive oxygen species (ROS), such as superoxide radicals ($\cdot O_2^-$) and hydroxyl radicals ($\cdot$OH). These non-selective, high-energy radicals react with targeted organic pollutants, such as synthetic dyes or antibiotics, breaking them down into transient intermediates before mineralizing them into harmless end products like H_2O, CO_2, and simple inorganic ions. To date, multiple SC photocatalysts for environmental pollutant degradation have been intensively studied. The wide Eg, stable, non-toxic metal oxides, e.g., titanium dioxide (TiO_2) (24) and zinc oxide (ZnO) (25), but restrict their activation to UV light. Bismuth-based multi-component oxides and oxyhalides, such as $BiVO_4$ (26) and BiOBr (27), show unique layered crystal structures causing internal electric fields (IEFs) to segregate charge carriers to better capture the visible spectrum. Despite their extensive usage, non-sulfide SC photocatalysts have fundamental restrictions that limit their efficiency. Such as fast e^-–h^+ recombination and activate mostly in the UV range, using merely 3%–5% of the solar spectrum. BiOBr has a layered crystal structure resulting in an IEF help for better charge separation, but its CB edge is thermodynamically too positive, depleting the reducing power of photogenerated e^-s required to drive key surface reactions like $\cdot O_2^-$ radical generation.

Metal sulfide-based SCs, including CdS, ZnS, In_2S_3, and MoS_2, are regarded as highly effective photocatalysts due to their favorable Eg and superior electronic properties (28–32). Many metal sulfide have a narrow Eg that results from S 3p orbitals (33), in contrast to broad bandgap metal oxides. This allows for effective absorption of visible light, which makes up around 43%–45% of sunlight, with a strong quantum size impact. Furthermore, compared to oxides and oxyhalides, these materials' CB edges are often much more negative (34). This property gives photogenerated e^-s significant reducing power, which allows them to support difficult processes like the evolution of hydrogen (H_2) and the destruction of pollutants. High charge-carrier mobility supports this increased thermodynamic driving force. The less electronegative sulphur (S^{2-}) anions provide a hybridized VB that facilitates rapid e-transport, hence reducing the harmful e^-–h^+ recombination bottleneck seen in other materials. However, photocorrosion, aggregate formation in aqueous conditions, leaching of hazardous metal ions, and quick recoupling of photogenerated e^-–h^+ couples are obstacles to the use of metal sulfide (35). Since the toxicity of inorganic nanostructured photocatalysts in wastewater treatment reactions is frequently disregarded, the environmental friendliness of metal sulfide photocatalysts should be evaluated not only on their degradation capacity but also on their subsequent impact on the treated water (36). After the photocatalytic process, recovering the catalyst is a significant difficulty since it is very hard to extract the full amount from the reaction solution (37). Specifically, traditional metal chalcogenide systems frequently have low reusability and need intricate recovery processes. Potentially hazardous metals can build up in the environment over time in the unrecovered portion of the treated effluent. For example, a study found (36) that harmful Cd^{2+} ions are released from CdS because of its poor photocorrosion

stability, while another study (38) found that around 20% of the cadmium leaches from CdS nanoparticles within a day. These suspended or dissolved metals can interact with different molecules and substrates found in natural water bodies and wastewater, where photo dissolution caused by sunshine speeds up the release of dangerous cadmium (39). As a result of their ongoing buildup, metal concentrations may rise over acceptable thresholds, poisoning the water (38). Therefore, the potential of secondary metal contamination must also be taken into account; a photocatalyst cannot be regarded as ecologically beneficial based just on its capacity to remove organic pollutants. Therefore, methods like immobilisation or protective coatings are needed to stop the catalyst from leaking into the environment and to get rid of any possible secondary contamination (40).

These limitations can potentially be restricted by synthesizing metal sulfide using a significant synthesis technique as well as modification techniques. For example, Li et al. used a hydrothermal technique to synthesize metal sulfides/MXenes abundant in sulfur vacancies (SVs) for the effective photocatalytic stimulation of peracetic acid (PAA) and removal of contaminants (41). The system demonstrated rates for tetracycline hydrochloride (TCH) degradation, which were 10 times better than the ZnCoS/PAA group. The extensively generated SVs, caused by the incorporation of Ti_3C_2 into ZnCoS, significantly enhanced activity by concurrently facilitating light absorption, photocharge separation, and PAA activation. Thus, preserving shape, structure, morphology, size, and defect states is an essential initial step in the synthesis of metal sulfides to ensure optimal performance. There are several methods that have been thoroughly addressed in the current review articles. Furthermore, the performance of the metal sulfide was improved through the utilization of various modification techniques such as doping (42), vacancy creation (43), heterojunction formation (44), etc., discussed in this review article. For instance, Song et al. efficiently produced CuS/ZnS and CuS/CdS composites from elemental powders despite the need for additional chemicals or solvents (45). The degradation efficiencies of methylene blue (MB) and rhodamine B by CuS/ZnS and CuS/CdS composites exceeded 95% after 30 min, whereas the degradation efficiency of methyl orange surpassed 85% in 90 min. Their photocatalytic qualities can be enhanced by quantum confinement phenomena, making them useful materials for dye degradation. Finally, we have discussed the use of metal sulfide or metal sulfide-based SC photocatalysts in environmental remediation, specifically their effectiveness in eliminating a variety of environmental contaminants. We have also highlighted prospects, emphasizing the need for more research to enhance other metal sulfide properties.

The first part of this research looks at the many kinds of pollutants that contaminate our environment and the harm they do to ecosystems. The intrinsic benefits of metal sulfide SC photocatalysis are then discussed in more detail. Synthetic techniques and modification tactics are described to increase catalytic activity. Additionally, a summary of the connection between active sites and photocatalytic applications in the metal sulfide-based pollution removal method is provided. Lastly, the main problems and difficulties related to metal sulfides are emphasized. This review aims to offer a comprehensive understanding of metal sulfides within the context of photocatalysis.

Properties of metal sulfides

Generally, the metal sulfides are composed of sulfur anions coordinated with metal cations and are classified into binary metal sulfides (CdS and SnS_2), ternary metal sulfides ($ZnIn_2S_4$), and polynary systems. They have emerged as considerable visible-light-responsive photocatalysts due to their distinctive electronic properties and light-harvesting capabilities. Their narrow band gap energies facilitate the extensive absorption across the visible region, thereby promoting the photogeneration of charge carriers for photocatalytic reactions (46). Notably, these photoinduced electrons accumulated in the CB of metal sulfides, thereby exhibiting strong reducing power. Additionally, these electrons participate in the reduction reaction owing to their electron-donating attributes while suppressing the electron-hole recombination. Simultaneously, this enhanced the charge separation and redox kinetics, thereby improving the potential of metal sulfides for photocatalytic applications (47). Furthermore, the quantum confinement effects of these materials offered tunable electronic properties, prolonged carrier lifetime, and efficient charge utilization, thereby enhancing the photocatalytic performance (48). For illustration, among the II-VI SC family, CdS has emerged as a visible-light-responsive photocatalyst owing to its narrow band gap (~2.4 eV), which ensures the efficient utilization of the solar spectrum, and a strongly negative CB (49). Generally, it consists of two phases: hexagonal wurtzite and cubic blende. Among these, the hexagonal wurtzite structure exhibited superior photocatalytic performance, attributed to its particle size, surface area, and enhanced adsorption properties (50). Moreover, integrating both phases into one photocatalyst promotes charge migration and efficient separation of charges (51). Another widely investigated metal sulfide photocatalyst is n-type SnS_2, with a narrow band gap (~2.1 eV), suitably sufficient for efficient solar light harvesting. Besides, it exhibited a layered crystal structure, where a tin layer is tightly confined within two sulfur layers, promoting charge separation, thereby enhancing photocatalytic efficiency (52, 53). In addition, among ternary metal sulfides, $ZnIn_2S_4$ comprises cubic, hexagonal, and trigonal crystal structures as represented in (**Figure 1**). Among these, hexagonal has been extensively studied, owing to its synthesis under mild conditions (54). Hexagonal $ZnIn_2S_4$ owns a narrow band gap (2.29 eV) and

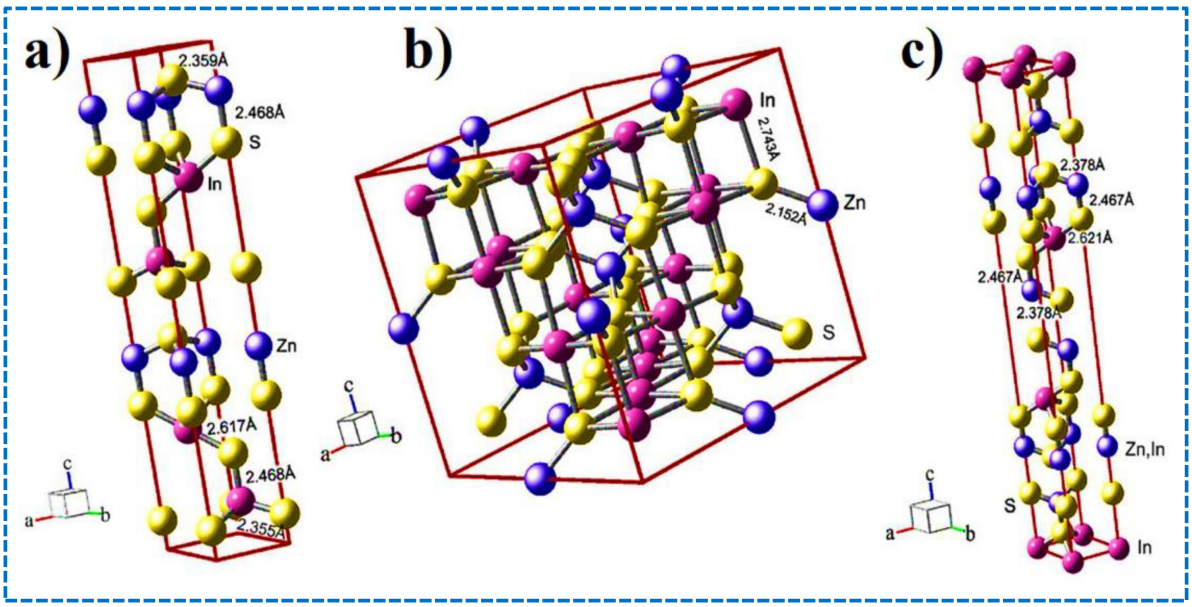


FIGURE 1 | Representation of the crystal structure of $ZnIn_2S_4$ polymorphs: **(a)** hexagonal, **(b)** cubic, **(c)** rhombohedral (54).

a unique S-Zn-S-In-S-In-S layered structure, efficient for photocatalytic performance (55, 56). Besides, the polynary metal sulfides, Cu_2ZnSnS_4, comprise a ZnS-derived-centerd tetragonal crystal structure. The lattice is characterized by each sulfur atom tetrahedrally coordinated by four metal cations, establishing a robust 3-D highly ordered atomic network (57). Overall, the results highlight the thorough comprehension of the basic characteristics of metal sulfides, improving the effectiveness of photocatalytic conversion and light absorption.

Photocorrosion mechanism and suppression strategies

Photocorrosion is a major obstacle for metal sulfide photocatalysts because the photo-generated charge carriers that eliminate pollutants also attack the SC lattice (58). For CdS-type sulfides, the primary mechanism is hole-induced oxidation: surface-accumulated holes oxidize lattice sulfide ions (S^{2-}) into elemental sulfur (S^0) and/or sulfate (SO_4^{2-}), causing the metal cation to leach into the solution and gradually destroying the active surface. This process is heavily dependent on dissolved oxygen. In an aerated aqueous medium, the overall corrosion reaction is $CdS + 2O_2 \rightarrow Cd^{2+} + SO_4^{2-}$, proceeding via $CdS + 4h^+ + 2H_2O + O_2 \rightarrow Cd^{2+} + SO_4^{2-} + 4H^+$. Conversely, in the absence of oxygen, only two holes are required, and the product is elemental sulfur ($CdS + 2h^+ \rightarrow Cd^{2+} + S$). This dependence on oxygen is directly relevant to wastewater treatment, where dissolved O2 is ubiquitous, causing the more destructive sulfate-forming pathway to dominate. Corrosion is also strongly pH-dependent: acidic media accelerate Cd^{2+} leaching, whereas alkaline conditions inhibit dissolution and stabilize the catalyst. Sacrificial agents (such as Na_2S/Na_2SO_3 or organic substrates acting as electron donors) mitigate corrosion by consuming photo-generated holes more rapidly than water does. This is because of their less positive oxidation potentials, thereby protecting the sulfide lattice (58, 59). However, the most robust strategy involves structural modifications such as heterojunction formation, doping, co-catalyst loading, and morphology or crystal engineering, all of which mitigate hole accumulation on the sulfide surface or stabilize the lattice. One example is the hybridization of CuS with an amino-functionalized Ti-based MOF, NH_2-MIL-125 (NM125), to create a Z-scheme heterojunction for photocatalysis under natural sunlight (60). ICP-OES monitoring of Cu^{2+} leaching revealed that pure CuS released 229 ppm of Cu^{2+} after 10 h of visible-light exposure, whereas NM125@CuS(9.1) released less than 6.78 ppm under identical conditions. This occurred because photogenerated electrons from the MOF recombine with holes in the CuS VB, and the released Cu^{2+} remains bound through coordination with amine groups. S 2p XPS analysis further confirmed this, as after 10 h of exposure, the content of elemental S^0 in pure CuS rose from 14% to 33% (due to the oxidation of S^{2-} by holes ($CuS + 2h^+ \rightarrow Cu^{2+} + S$). Whereas in NM125@CuS(9.1), it increased only from 8% to 10%, which is direct evidence of the suppression of hole-induced photocorrosion within the heterostructure. Another approach involves the Ag-mediated Z-scheme NiO/Ag/CdS heterojunction, where Ag nanoparticles at the NiO/CdS interface act as an electron-transfer bridge (61). This facilitates interfacial recombination between holes generated in the CdS VB and electrons arriving from the NiO CB, thereby completely suppressing the self-oxidation of CdS. Cyclic durability testing confirmed this protection: after 9 h of continuous reaction (three cycles), the NiO/Ag/CdS

composite retained 88.1% of its initial hydrogen-production activity, whereas pure CdS retained only 21.9% due to severe photocorrosion. Post-durability XRD analysis revealed no significant changes in the position or intensity of diffraction peaks, confirming the stability of the crystal structure. SEM imaging showed that the 1D rod-like CdS morphology and the composite structure with NiO remained intact, showing no signs of aggregation or corrosion. Overall, these studies confirm that heterojunction engineering is an effective and general strategy for creating durable, photocorrosion-resistant metal sulfide photocatalysts by extracting holes from the sulfide lattice. Overall, this mechanistic and spectroscopic information demonstrates that the photocorrosion of metal sulfides is driven by hole-mediated sulfide oxidation, controlled by pH, dissolved oxygen, and sacrificial agents and can be effectively prevented through appropriate heterostructure design.

Synthesis methods

Different synthesis methods have been used to prepare the metal sulfides, which have different compositions, morphologies, and structural properties. The synthesis pathway is of great importance to the physicochemical properties of the product sulfides and therefore their potential uses. These include commonly used methods such as hydrothermal, solvothermal, co-precipitation, chemical vapor deposition (CVD), microwave-assisted, and other solution- or vapor-based methods. The following sections discuss these synthesis methods and highlight representative studies reported for the preparation of metal sulfide materials.

Hydrothermal method

One of the most often used methods for preparing metal sulfides is the hydrothermal process, which makes it possible to create nanostructured materials with a variety of surface morphologies and significant porosities. The basic steps are the dissolution of metal salts and a sulfur compound in an aqueous solution and the transferring of the reaction mixture into a closed Teflon-lined autoclave. At elevated temperatures, the sealing reaction system promotes the nucleation and growth of the metal sulfide structure (62). The adaptability of the physicochemical characteristics of the final products, which may be accurately modified by adjusting the synthesis settings, is a unique advantage of this approach. The reaction temperature, the pH, the pressure, and the reaction time can have a critical influence on the growth behavior of the material and consequently its morphology. Therefore, the hydrothermal method has been widely used to prepare metal sulfides with structural parameter control. As a representative example of hydrothermal synthesis,

Peng et al. reported the preparation of montmorillonite-supported MoS_2/CdS heterostructure (Mt@MoS_2/CdS) by directly growing MoS_2 nanosheets (NSs) and CdS nanoparticles on the surface of montmorillonite by the hydrothermal method. Typically, sodium molybdate, cadmium acetate, and thioacetamide were dissolved in the deionized water (DIW), and montmorillonite was added to the mixture (63). The obtained suspension was transferred to a Teflon-lined autoclave and autoclaved at 200 °C for 24 h. The final Mt@MoS_2/CdS-7 composite was achieved after washing and drying. An illustration of the hydrothermal synthesis process is shown in **Figure 2a**. Herein, SEM analysis of MoS_2/CdS-7 revealed agglomerated heterostructure particles of varying sizes, with MoS_2 grown on the CdS surface. The TEM also showed that CdS nanoparticles were coated by MoS_2 NSs (**Figure 2b**). Furthermore, TEM and HRTEM images of Mt@MoS_2/CdS-7 (**Figure 2c**) showed that montmorillonite-assisted hetero-assembly of MoS_2 nanosheet and CdS nanoparticle resulted in smaller particle size and better dispersion than that of MoS_2/ CdS-7. The photocatalytic performance was estimated by the degradation of Rhodamine B under visible light, in which Mt@MoS_2/CdS-7 showed 98.8% degradation in 45 min.

In another method, Mulu et al. prepared MoS_2 NSs through a facile and green hydrothermal approach using L-cysteine as both the sulfur source and capping agent (64). A typical synthesis involved dissolving 2.0 g of (NH4)·Mo_2O_{24}·4H2O and 4.0 g of L-cysteine in 50 mL of DIW, then sonicating the mixture for 30 min to get a clear solution. The resulting mixture was subsequently transferred into a 100 mL stainless-steel autoclave and heated at 200 °C for 12 h. The hydrothermal treatment facilitated the formation of layered MoS_2 structures, while the use of L-cysteine as the sulfur precursor provided a greener synthetic route. The morphology of the obtained product was examined using SEM and TEM analyses. SEM images (**Figures 2d, e**) revealed an aggregated surface with a relatively rough texture, whereas TEM observations confirmed the formation of sheet-like MoS_2 NSs. Furthermore, the TEM images demonstrated the presence of few-layered and aggregated MoS_2 structures synthesized through the hydrothermal process.

In general, the reported studies have demonstrated the efficiency of the hydrothermal method to synthesize metal sulfides and heterostructures based on them of various shapes. These composites of MoS_2 and MoS_2/CdS supported on montmorillonite have been successfully made, and the method offers great flexibility for the preparation of photocatalytically active metal sulfide materials.

Sol-gel method

The sol-gel method is regarded as one of the simplest and most widely utilized approaches for the synthesis of

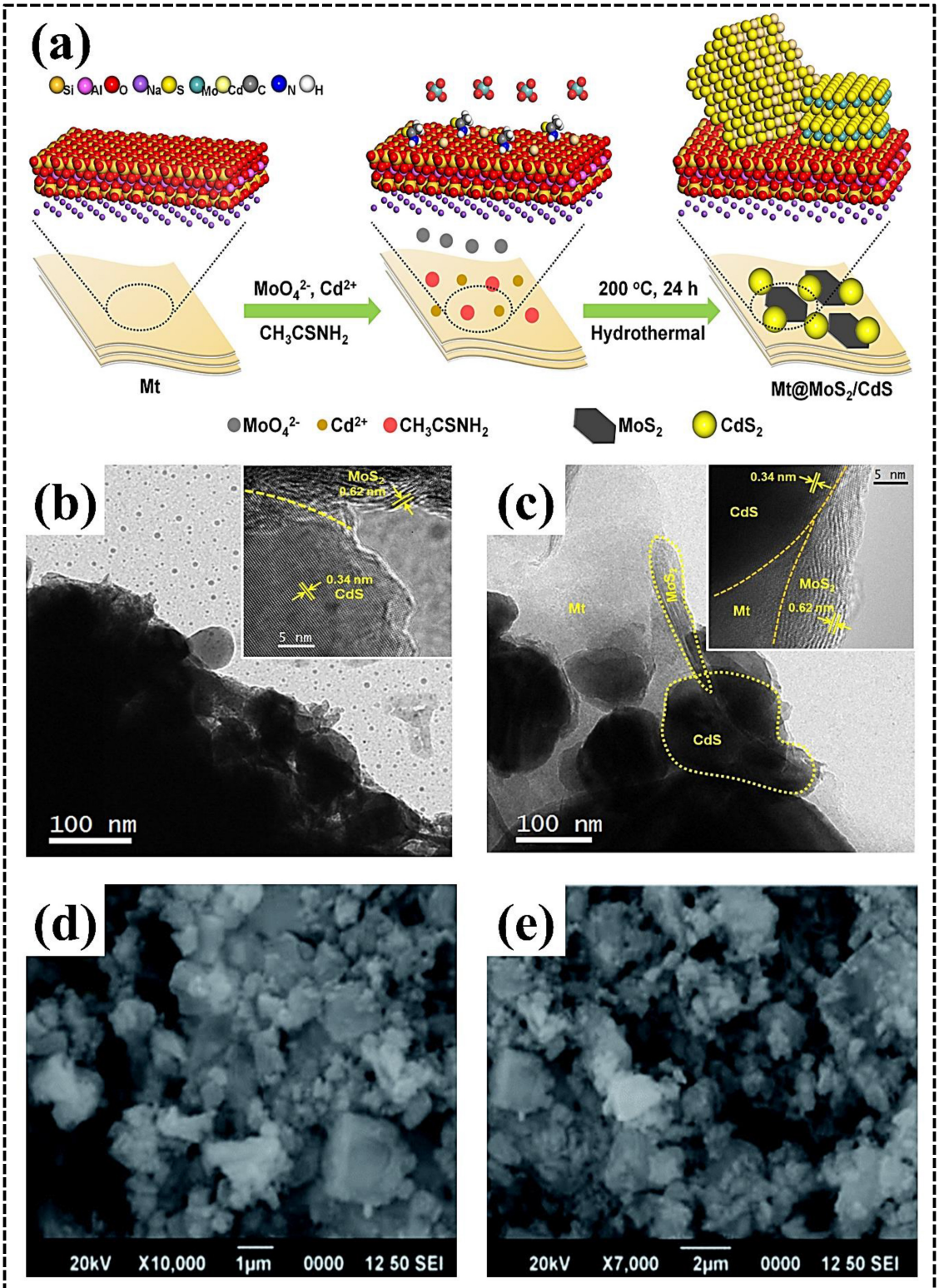


FIGURE 2 | (a) Schematic illustration depicting the hydrothermal synthesis process of Mt@MoS_2/CdS. TEM images of **(b)** MoS_2/CdS-7 and **(c)** Mt@MoS_2/CdS-7 provide insight into the morphology of the synthesized composites (63), and **(d, e)** present representative SEM images of the NSs recorded at different magnifications, highlighting their morphological features (64).

metal sulfides. The technique involves the transformation of the metal sulfide sol to a gel network by forming metal-sulfur-metal linkages that are then dried to form the required material. The synthesis is generally achieved by dissolving a metal salt precursor in an appropriate solvent and subsequently slowly adding a sulfur source (usually

sodium sulfide) to drive the formation of the sol (46). The porous metal sulfides can be prepared under relatively simple conditions as a result of the controlled transformation of the sol into the gel. Besides the preparation of pure materials, the sol-gel method is also well suited to incorporate both metal and non-metal dopants; hence, it is a versatile method for the tailoring of the properties of metal sulfides. Owing to its simplicity and adaptability, a variety of metal sulfide photocatalysts have been prepared using the sol-gel process, as illustrated by the representative studies discussed below. In this context, Singh et al. employed a sol-gel approach to fabricate Ag-CdS@Pr-TiO_2 core-shell nanoparticles, where Ag-doped CdS functioned as the metal sulfide core and Pr-TiO_2 constituted the shell layer. The synthesis started by dispersing 1 g of Ag-doped CdS nanoparticles in ethanol and then adding drop by drop a mixture of TiO_2 and $Pr_2(SO_4)_3$ solution (65). The suspension was then aged for 20 h to promote the formation of the core-shell structure. The product was later separated by centrifugation and was carefully washed to remove remaining impurities and dried at room temperature and ground into fine powder to get the final Ag-CdS@Pr-TiO_2 composite. In order to investigate the structural and morphological characteristics of the synthesized material, a variety of methods were employed. However, the XRD analysis showed the formation of highly crystalline nanoparticles, and the SEM images (**Figures 3a, b**) showed that the particles were mostly spherical with a certain amount of agglomeration and incomplete separation. Based on the reported observations, the size of the particle was between 10 and 30 nm. Moreover, HRTEM analysis is also used to gain further insight into the morphology and successfully confirmed the formation of the core-shell architecture as shown in (**Figures 3c, d**). The Ag-CdS@Pr-TiO_2 nanoparticles' photocatalytic activity was examined by the degradation of methyl orange under visible-light illumination. The synthesized composite showed effective photocatalytic performance with complete discoloration of the dye in 30 min and can be used for photocatalytic activity under visible light.

In another work, Sankar et al. prepared Ni-doped CdS nanoparticles using the sol-gel technique with different Ni concentrations (0.5%, 1.0%, 1.5%, and 2.0%) to find the effect of Ni incorporation on the structural, optical, and morphological properties of CdS. The synthesis was performed by the preparation of a cadmium precursor solution containing 0.15 M of cadmium acetate in methanol, and then a second solution containing 0.15 M of nickel chloride in water was prepared. The nickel precursor solution was slowly introduced into the cadmium solution and stirred continuously for 85 min until a homogeneous and close-to-transparent solution was formed (66). The precipitate obtained was washed, filtered, dried at 100 °C for 24 h and then sintered at 450 °C for 2 h to get the final Ni-doped CdS nanoparticles. Average crystallite sizes of synthesized samples were in the range of 8.70–9.93 nm. SEM analysis of the Ni (1.5%) doped CdS sample (**Figures 3e, f**) revealed a combination of rod-like and cube-like structures with unequal grain sizes in the range of 12–35 nm. HRTEM was also used to gain further insight into the morphology, and the Ni-doped CdS nanoparticles showed a spherical morphology. The HRTEM observations also confirmed the formation of porous spherical clustered nano-assemblies. In addition, optical characterization revealed a gradual decrease in band-gap energy from 2.36 to 2.29 eV with increasing Ni doping concentration.

The above-mentioned studies illustrate the flexibility of the sol-gel technique to prepare materials based on metal sulfides in different compositions and architectures. The synthesis of core-shell nanoparticles and doped nanostructures is the realization of the potential use of this approach to the structural and optical tailoring of metal sulfides.

Chemical vapor deposition method

Chemical vapor deposition is an extensively used vapor-phase synthesis technique in which the formation of a solid is achieved by a chemical reaction between gaseous reactants on or near a heated surface of the substrate (67). The solid material formed can be deposited as a thin film, powder, or even a single crystal, and its properties can be adjusted by changing the substrate material, the substrate temperature, the composition of the reaction gas, the total pressure during the deposition, and the conditions of the gas flow. One of the key benefits of CVD is its excellent throwing power and allows for uniform and property coatings on complex geometries, even. Moreover, the technique provides the ability to deposit selectively or locally onto patterned surfaces (68). Because of these merits, CVD has become an attractive process for the production of advanced functional materials. Specifically, it is now widely used for the synthesis of high-quality two-dimensional transition metal sulfides and other metal sulfide systems of well-controlled morphology and crystallinity. In this direction,

Fu et al. synthesized a flower-like Cu_2O@CuS core-shell composite through a two-step strategy involving hydrothermal preparation of Cu_2O followed by in-situ CVD sulfurization (**Figure 4a**). This method involved pre-synthesizing Cu_2O and then treating it with sulfur vapor at 200 °C under an N2 atmosphere, which resulted in in situ growth of a CuS shell on the Cu_2O surface (69). A series of Cu_2O@CuS composites were obtained by varying the Cu_2O-to-sulfur mass ratio during the sulfurization process. SEM observations revealed that the pristine Cu_2O possessed a well-defined hexapetalous flower-like morphology with a smooth surface (**Figure 4b**). Following the CVD treatment, CuS was successfully deposited onto the Cu_2O surface in the form of stacked NSs, forming a distinct core-shell architecture while preserving the overall flower-like structure (**Figure 4c**). The formation of the CuS shell not only changed

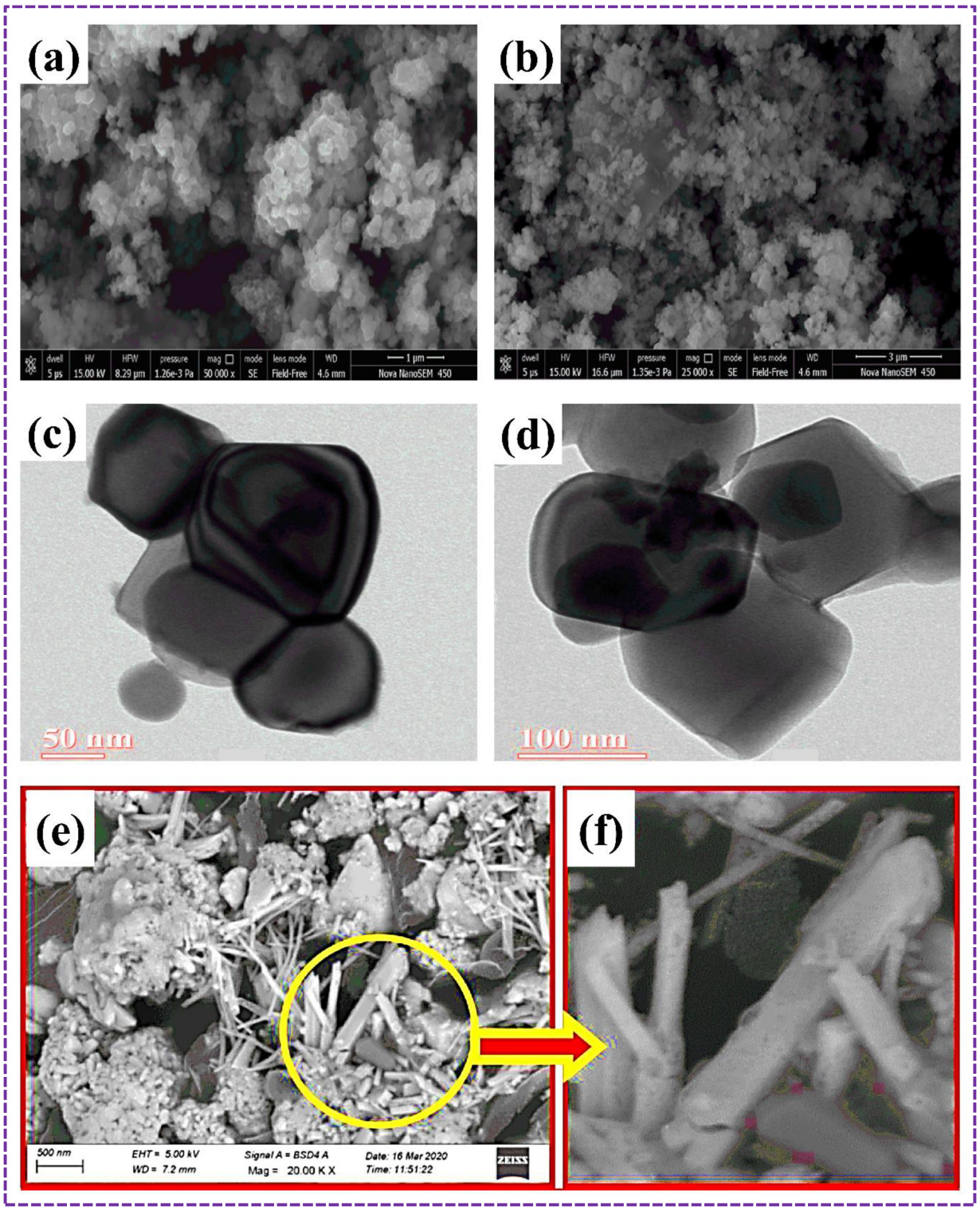


FIGURE 3 | (a, b) represents the SEM images of Ag-CdS@Pr-TiO_2 core/shell nanoparticles, highlighting their surface morphology. **(c, d)** Show the HRTEM images of the Ag-CdS@Pr-TiO_2 nanocomposite recorded at different magnifications, providing further insight into the nanostructural features of the material (65). **(e, f)** Represent the SEM images of Ni (1.5%) doped CdS nanoparticles, illustrating the morphological characteristics of the doped CdS system (66).

the surface morphology but also provided light absorption and better separation of the charge carriers generated by the light to enable better separation. The study showed that in-situ CVD sulfurization can be an effective method to prepare the Cu_2O@CuS core-shell photocatalysts with higher activity and stability.

Furthermore, Buckingham et al. synthesized CdS thin films using aerosol-assisted chemical vapor deposition

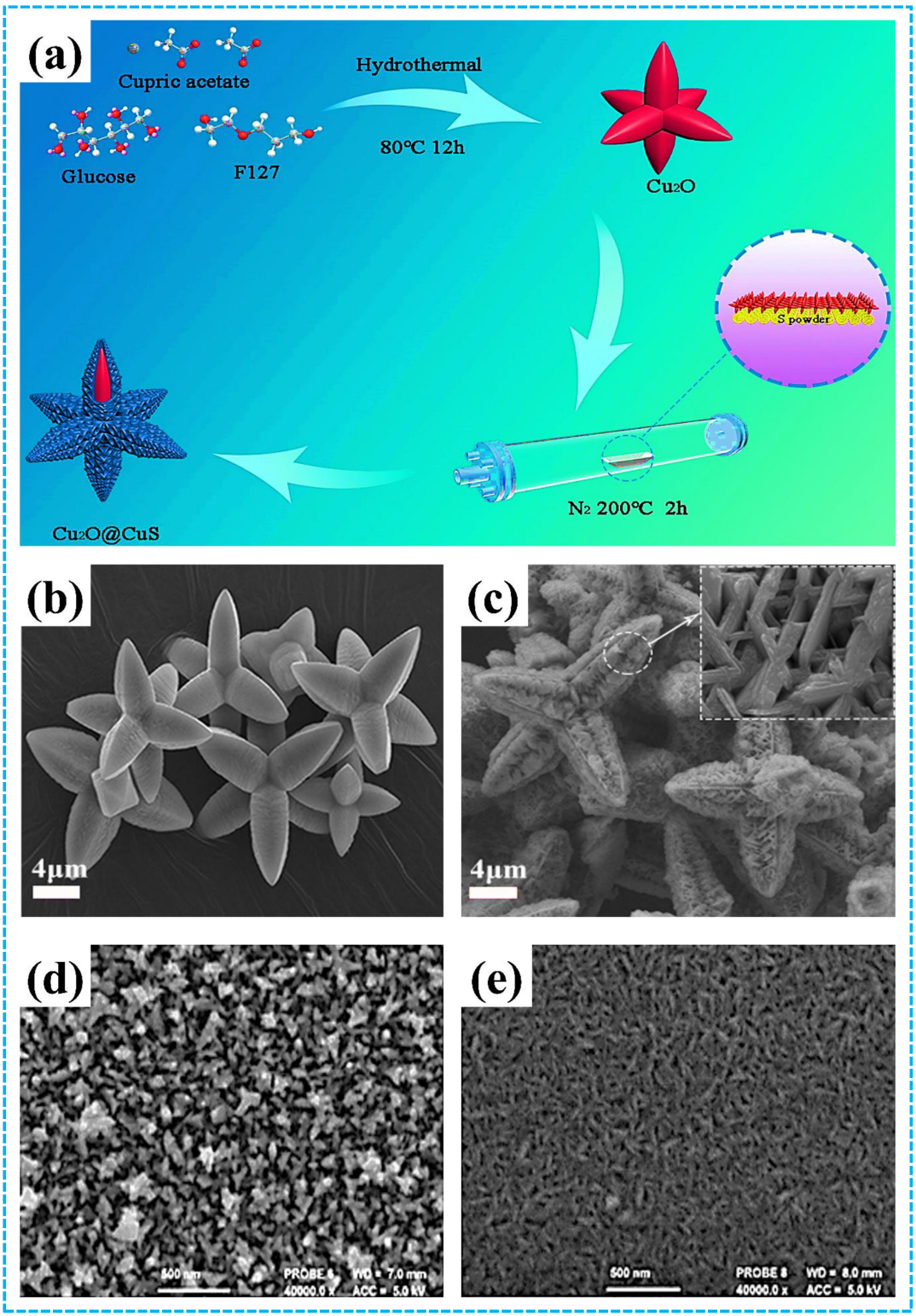


FIGURE 4 | (a) Illustrates the synthesis route employed for the preparation of Cu_2O@CuS composites. High-resolution SEM images of **(b)** Cu_2O and **(c)** Cu_2O@CuS-3 depict the morphological evolution following the formation of the CuS shell (69), and **(d, e)** present representative SEM images of CdS films deposited on glass substrates via AACVD from complex 3 at 220 and 350 °C, respectively, demonstrating the morphology of the resulting CdS films under different deposition temperatures (70).

(AACVD) from cadmium (II) ethyl xanthate-based single-source precursors. Both the deposition temperatures, 220 and 350 °C, led to the formation of crystalline CdS films on silica-coated glass substrates (70). The morphology of CdS was found to be very sensitive to the deposition processes, as shown by SEM analysis. When CdS films were prepared

using precursor compound 3-methylpyridine, the resulting CdS film was found to have a dense, plate-like structure at 220 °C (**Figure 4d**). A similar morphology was retained at 350 °C, where the plates became more compact and well-defined (**Figure 4e**). These films had a greater density of surface features and crystallinity than their counterparts made from the other precursors. Powder X-ray diffraction additionally confirmed the creation of hexagonal CdS, and crystallite dimensions of about 30 nm were reported for films from the 3-methylpyridine precursor. The optical band gaps of the deposited CdS films ranged from 2.25 to 2.40 eV, which is comparable to bulk CdS properties. The study showed that AACVD is a suitable method for the formation of highly crystalline CdS films with customizable morphology, with the 3-methylpyridine precursor demonstrating an ability to form dense, well-crystalline, plate-like CdS film structures.

Modification strategies

Heterojunction formation

Metal sulfide-based photocatalysts have been widely investigated due to their high visible light absorption property and adjustable electronic structure. But their practical uses in photocatalytic reactions are still limited by several major challenges, such as the high recombination rate of photogenerated charge carriers, low utilization of solar light, photocorrosion, complex catalyst recovery from water-based reaction systems, and high operational cost (71–73). To overcome these drawbacks, heterojunction engineering has become an efficient and sustainable approach to improve the photocatalytic activity. The generation of heterojunctions of metal sulfides with other SCs can widen the light absorption spectrum and also facilitate the efficient separation and migration of the charge on the interface, thus enhancing the photocatalytic efficiency for environmental treatment and solar energy conversion (74). There are three types of typical heterojunctions based on the charge transfer mechanism and band alignment: heterojunction of Type-I (straddling gap), Type-II (staggered gap), and Type-III (broken gap). Of them, Type-II heterojunctions have been widely investigated in the field of photocatalysis due to their ability of spatial charge separation, which is beneficial for extending the lifetime of charge carriers generated by photons. However, in type-II systems, the stepwise movement of electrons and holes usually reduces the redox ability of the photocatalysts, and this is the reason why they are less efficient in photocatalytic reactions with high energy demands (75). To address these limitations, more complex heterojunctions like Z-scheme and S-scheme photocatalysts were then created (76). These systems maintain high redox potentials and, at the same time, allow for effective charge separation, resulting in higher photocatalytic activity than conventional heterojunction systems (77).

Type II heterojunction

Based on their efficient charge separation capability, Type-II heterojunctions, with 1D/1D, 0D/1D, and 1D/2D architectures, are the most widely studied heterojunction systems for photocatalysis (78, 79). In this case, under light illumination, the photogenerated electrons in the CB of SC 1 travel to the CB of SC 2, and the holes generated in SC 2 travel to the VB of SC 1. This interfacial charge migration results in an IEF between the two SCs, and the IE field is good for suppressing electron-hole recombination. The spatial separation of charge carriers is thus increased significantly, which results in better photocatalytic activity and better performance of the photocatalytic reaction (80, 81). In Type-II heterojunctions, however, charge transfer is frequently hindered by migration of similar charge carriers that can affect the driving force at the interface and the effective redox capability of the photocatalytic system (82).

For instance, $ZnMoS_4$ (ZMS) was coupled with CdS via simple physical stirring to form a Type-II heterojunction photocatalyst for visible-light-driven hydrogen evolution (83). Photocatalytic performance evaluation showed an outstanding improvement in the production of hydrogen after the formation of a heterojunction. The pristine CdS gave 48.13 μmol of H_2 under the visible-light irradiation for 5 h, while the pure ZMS showed relatively low activity with 9.51 μmol of H_2 generation. However, the CdS/ZMS composite exhibited a much higher yield of hydrogen evolution of 292.31 μmol, which is almost six times and 31 times higher than that of CdS and ZMS, respectively. Furthermore, it was found that the optimization of the sacrificial agent showed that lactic acid was the best hole scavenger, which led the composite to reach its best hydrogen production performance. The stability behavior of the composite also verified its good durability, with no deactivation being seen in the first few cycles of photocatalytic cycles (in consecutive long-term operation). This improved photocatalytic activity is mainly attributed to the effective charge transfer at the interface between the two materials, that is, due to the heterojunction structure of Type-II. The Mott-Schottky measurements showed that both CdS and ZMS were n-type SCs with the CB potential of −0.99 eV (vs. SHE) and −1.06 eV (vs. SHE), respectively. This arrangement of the bands was staggered to allow for the movement of electrons in a direction across the interface, which led to an effective separation of charge and reduced the electron-hole recombination. The Kubelka-Munk analysis showed that the bandgap energy of CdS was 2.15 eV and that of ZMS was 1.70 eV, confirming the effectiveness of incorporating ZMS in the bandgap reduction and broadening of light utilization in the solar spectrum. Additionally, electronic structure modulation due to the heterojunction formation was confirmed by the density functional theory (DFT) calculations. Although DFT calculations tend to underestimate the bandgap, the

theoretically calculated value of CdS was found to be 1.1 eV, lower than the value obtained from the UV-Vis analysis of 2.15 eV. Also, the theoretical bandgap was narrower than the experimental bandgap of ZMS (1.70 eV). The density of states (DOS) analysis revealed that the DOS near the Fermi level of CdS mainly comes from the hybridized s- and p-orbitals, while the DOS near the Fermi level of ZMS mainly comes from d- and p-orbitals related to Mo species. The work function calculations showed that the work function of CdS was 5.2 eV while that of ZMS was 4.3 eV for the (220) facet, indicating the higher Fermi level in ZMS. This led to spontaneous electron migration from the ZMS to CdS, which led to formation of an IEF at the heterointerface that helped increase charge separation and carrier transfer. With visible light irradiation, an electron from ZMS was transferred to CdS successfully, which not only decreases the charge recombination but also enhances the number of active surface sites for proton reduction. Thanks to the enhanced visible-light absorption, optimized band alignment, and efficient charge separation, the CdS/ZMS Type-II heterojunction photocatalyst exhibited high hydrogen evolution activity, highlighting the potential of heterojunction engineering for solar-based hydrogen generation.

In another work, Wang et al. investigated the photocatalytic hydrogen evolution performance of novel metal sulfide/UiO-66-NH_2 heterojunctions under solar-light irradiation (84). The effects of different metal sulfides (CdS, Bi_2S_3, and ZnS) on the structural, optical, and photocatalytic properties of heterojunctions were investigated. The successful heterojunction formation was verified by the XRD analysis, which showed that the metal sulfides maintained the crystalline framework of UiO-66-NH2. TEM revealed that CdS nanoparticles had a uniform dispersion on the surface of UiO-66-NH_2, and HRTEM also revealed the lattice fringes of 3.36 Å and 2.91 Å, which matched the lattice plane (111) and (200) of CdS. The tests for hydrogen evolution under the photocatalytic conditions showed that there was a considerable difference in the catalytic activity between the heterojunctions. In the case of the ZnS/UiO-66-NH_2 system, only a small amount of hydrogen was produced, while the CdS/UiO-66-NH_2 system produced hydrogen at a rate of 64.0 μmol g^{-1} h^{-1}. In contrast, the pristine CdS had hydrogen production activity of 8.0 μmol g^{-1} h^{-1}, which represents almost eight times the production activity of the heterojunction photocatalyst. This improvement was attributed to the strong interfacial interactions between CdS and UiO-66-NH_2, which facilitate efficient charge separation and transfer. The Mott-Schottky analysis revealed that both materials exhibited an n-type SC behavior and that the UiO-66-NH_2 had a lower flat band potential of −0.71 V compared to the CdS (−0.87 V). Hence, they showed that their CB potentials are −0.51 and −0.67 V, respectively, which indicates a Type-II heterojunction mechanism. The electrons in the CB of CdS were rapidly transferred to UiO-66-NH_2 and enabled efficient proton reduction to hydrogen upon light irradiation. Concurrently, the holes within the UiO-66-NH_2 were transferred towards the VB of CdS. This charge separation reduced the recombination and further improved the photocatalytic hydrogen evolution activity of the CdS/UiO-66-NH_2 system.

Z-scheme heterojunction

The potential of Z-scheme heterojunctions as highly efficient photocatalytic systems has been found due to effective charge transfer and maintaining strong redox capability. Unlike conventional Type-II heterojunctions, the Z-scheme mechanism facilitates low-energy charge carrier recombination and keeps highly reductive electrons and strongly oxidative holes, which improves photocatalytic activity. First, the traditional liquid-phase Z-scheme systems were invented, where two SCs were used but were not directly in contact with each other but rather with a reversible electron acceptor/donor (A/D) redox mediator. In these systems, charge transfer took place by redox reactions between electron acceptors and donors, allowing the migration of the photogenerated electrons and holes between the SCs without their direct contact (85). Although the traditional liquid-phase Z-scheme systems exhibited enhanced charge transfer characteristics, there existed several limitations, namely pH sensitivity, back reaction of redox reaction, light shielding due to redox mediator, and limited application in the liquid phase. Therefore, subsequently, all-solid-state (ASS) Z-scheme heterojunctions were developed to overcome these limitations. To enhance the efficiency of charge separation and increase the speed of charge transfer across the interfaces in ASS Z-scheme systems, solid electron mediators like noble metals or conductive materials were introduced between SCs. The use of electron mediators, however, brought some disadvantages, such as the high cost of materials, shielding of incident light, and complicated fabrication processes, which limited their practical application on a large scale (86–88).

To simplify the structure of the system and improve the photocatalytic efficiency, direct Z-scheme heterojunctions were fabricated (86, 89, 90). These systems allow for direct electron transfer between two SCs without any external electron mediators because of the close contact of the two SCs. The electrostatic attraction between oppositely charged carriers facilitates fast charge transfer and helps to minimize unwanted reactions, which will decrease the fabrication costs. Consequently, the metal sulfide photocatalysts are being focused on for the production of hydrogen, the reduction of CO_2, and the degradation of pollutants. But factors such as incomplete photocarrier recombination and reduced quantum efficiency during continuous illumination remain a problem.

For instance, the researchers created nanoarray heterostructures of ZnO/MoS_2 on porous Ni foam and showed that the photocatalytic degradation of the sunlight was improved under a piezoelectric field (91). The lattice parameters and crystal structure of ZnO and MoS_2 are almost the same, which allowed the formation of a stable heterojunction with low lattice mismatch. The successful incorporation of Zn, O, Mo, and S species was confirmed by XPS analysis, and the BET analysis showed that ZnO/MoS_2 had a larger surface area due to the incorporation of the species, which has more active sites for the photocatalytic reactions. The heterojunction of ZnO/MoS_2 showed the best performance for the degradation of organic pollutants by the piezo-photocatalytic technique. The degradation efficacy of MB and Congo red (CR) under light irradiation was greatly improved from 45.3% and 24.1% to 71.9% and 76.6%, respectively, with the addition of the stirring-induced piezoelectricity. The researchers suggested that the conventional Type-II heterojunction was converted into a direct Z-scheme system, which enhanced charge separation and maintained good redox properties. The MoS_2, having a lower work function (~4.52 eV), and bandgap (1.8 eV) absorbed the visible light, while the ZnO, having a high work function (~5.2 eV) and bandgap (3.37 eV) absorbed UV light. When the interfaces come into contact, band bending and heterojunction formation are caused by electron redistribution. The migration of photogenerated electrons and holes across the interface upon light illumination worked to reduce charge recombination. Additionally, the obtained highly reactive charge carriers from the piezoelectric field-assisted direct Z-scheme pathway facilitated the significantly superior photocatalytic degradation performance. Apart from spontaneous formation and stabilization of Z-scheme heterojunctions of SCs, researchers discovered that Z-scheme systems with efficient formation and stabilization could also be formed using some sacrificial agents.

For instance, Hao et al. synthesized a CdS/ZnS heterojunction photocatalyst containing Zn vacancies through an in-situ strategy using CdS/MOF-5 as a sacrificial template in the presence of Na_2S and Na_2SO_3 solutions (92). It was concluded that the creation of the Zn vacancy had a significant effect on controlling the charge transfer and increasing the photocatalytic hydrogen evolution activity. Photogenerated electrons of ZnS recombined with the holes in CdS via intimate ohmic contact, and the remaining electrons were then transferred to the Zn-vacancy defect states in ZnS. It was noted that this charge-transfer pathway was able to facilitate the separation of the electron and hole and prevent the photocorrosion of CdS. This means that the electrons produced by the photoexcitation of CdS are held in the CB without recombining, and they were able to catalyze the reduction of H^+ ions to H_2. Moreover, the ZnS structure deficient in Zn allowed for the creation of new electron transfer paths via two-photon absorption processes, enhancing charge migration even further. At the same time, the holes created in the VB of ZnS were quenched by the sacrificial electron donors (Na_2S and Na_2SO_3), helping to suppress the charge recombination and improving the stability of the heterojunction photocatalyst. Consequently, the CdS/ZnS Z-scheme heterostructure proved to have excellent photocatalytic activity and improved photo stability, emphasizing the significant importance of defect engineering and sacrificial-agent-assisted charge regulation in new-generation metal sulfide-based Z-scheme photocatalytic systems.

In other work, Ouyang et al. developed a layered core-shell $ZnIn_2S_4$@MoO_3 direct Z-scheme heterojunction for the visible-light-driven degradation of TCH in aqueous media (93). The researchers noted that, under visible-light irradiation, the heterostructured photocatalyst showed a considerably higher photocatalytic activity, the reason for which was mainly attributed to the efficiently working direct Z-scheme charge-transfer mechanism at the heterointerface. The enhanced photocatalytic behavior was attributed to the IEF that was created between $ZnIn_2S_4$ and MoO_3 upon contacting them together. The photogenerated electrons in the CB of MoO_3 rapidly recombined with the holes in the VB of $ZnIn_2S_4$ via the direct Z-scheme pathway. Hence, the VB of MoO_3 contains holes with high oxidizing power and the CB of $ZnIn_2S_4$ contains electrons with strong reducing properties. The researchers discovered that this selective charge recombination process was able to significantly achieve spatial charge separation and that the lifetime of the photogenerated carriers and that the redox capability of the heterojunction system was preserved. Therefore, the direct Z-scheme photocatalyst $ZnIn_2S_4$@MoO3 exhibited an excellent visible-light photocatalytic degradation efficiency towards the TCH pollutant. The studies taken together showed that the Z-scheme heterojunctions can greatly improve the separation of charge carriers, expand visible light absorption, and retain highly active redox active sites, and have shown tremendous potential for advanced photocatalytic applications. Due to the intrinsic limitations of conventional type-II and Z-scheme heterojunction systems, S-scheme heterojunctions have been developed in recent years as a new and very efficient approach in photocatalytic strategies involving metal sulfide material systems.

S-scheme heterojunction

In an S-scheme heterojunction, two SCs with different work functions are directly connected, and an interfacial band bending and an IEF are spontaneously formed in the heterojunction (94). This irregular band structure allows the selective recombination of photogenerated electrons and holes with lower redox potentials at the heterointerface via coulombic interactions, whilst maintaining very reductive electrons and very oxidative holes with high redox potentials (76, 95, 96). Consequently, S-scheme

metal sulfide heterojunctions effectively combine efficient charge separation with strong photo-redox capability, thereby overcoming the drawbacks of conventional Type-II systems that generally suffer from weakened redox strength after charge migration. Furthermore, the built-in electric field significantly accelerates directional charge transfer, suppresses electron–hole recombination, and prolongs the lifetime of photogenerated carriers (97–99).

For instance, Zhou et al. synthesized a 2D/2D $ZnIn_2S_4/Bi_4Ti_3O_{12}$ S-scheme heterojunction through a low-temperature solvothermal approach, in which $ZnIn_2S_4$ NSs were uniformly grown on the surface of flaky $Bi_4Ti_3O_{12}$ (100). The staggered band alignment between $ZnIn_2S_4$ and $Bi_4Ti_3O_{12}$ was found to be beneficial for the formation of an efficient charge-transport pathway in the S scheme. In this mechanism, the electrons generated by the photons were left in the CB of $ZnIn_2S_4$, and the holes were left in the VB of $Bi_4Ti_3O_{12}$ at the hetero interface. Hence, efficient charge separation and strong redox capability of the heterojunction were maintained to ensure the high tetracycline (TC) degradation performance in the visible-light illumination. A heterojunction of $ZnIn_2S_4Bi_4Ti_3O_{12}$ was prepared to optimize the removal efficiency of TC to be about 82.1% in 60 min, with a reaction rate constant about 6.8 times higher than that of pristine $ZnIn_2S_4$.

In a similar study, Su et al. studied an S-scheme quantum dots (QDs)/monolayer Bi_2WO_6 heterojunction using DFT calculations and experimental synthesis (101). Next, the CdS quantum dots were in situ hydrothermally combined with Bi_2WO_6 monolayers to form the heterostructure photocatalyst. They discovered that introducing Bi-S bonds at the interfaces between CdS quantum dots and Bi_2WO_6 monolayers was a key step for enabling the transfer of charges between them. The S-scheme heterojunction that was formed significantly facilitated the separation of charge carriers generated by the light and promoted the migration of the electrons and holes, resulting in the improvement of the photocatalytic activity while keeping the strong redox ability of the photocatalytic material. The results showed the importance of the interface engineering and S-scheme charge transfer pathway in enhancing the photocatalytic activity of the metal sulfide-based heterostructures. The S-scheme and Z-scheme heterojunctions share the same charge transfer mechanism and are aimed at achieving effective charge carrier separation to achieve high photocatalytic activity. In general, heterojunctions are formed from two SCs with appropriate Fermi level positions and both n-type. Specifically, heterojunctions are typically made of two appropriately matched n-type SCs whose Fermi level positions differ. In practical photocatalytic studies, it is not always possible to differentiate S-scheme systems from Z-scheme heterojunctions due to their similar charge-transfer pathways. However, the two heterojunction structures can achieve the spatial separation of the photo-generated electrons and holes, reduce the recombination of the electrons and holes, and greatly enhance the photocatalytic activity.

Application

Dye degradation

The diversity and complexity of organic pollutants found in wastewater are far greater than those of inorganic pollutants (102). Among these, pharmaceuticals and personal care products (PPCPs), organic dyes, and major environmental pollutants are particularly problematic. Handling dye-laden wastewater is challenging due to its high Chemical Oxygen Demand (COD) and Biological Oxygen Demand (BOD), as well as the presence of chemicals that do not degrade easily. Releasing organic dyes into aquatic ecosystems not only alters the water's color but also obstructs sunlight penetration, reduces dissolved oxygen levels, and disrupts the ecological balance. Thus, there is a need for efficient and sustainable approaches or methods to mitigate these emerging issues. For instance, Dharamalingam et al. demonstrated that the photocatalytic breakdown of MB dye was significantly enhanced upon exposure to UV-visible light (103). This enhancement resulted from a hydrothermal technique that transformed bulk MoS_2 into nanosheets (MoS_2-SDS NS) using sodium dodecyl sulfate (SDS) (**Figure 5a**). Due to quantum confinement effects, the surfactant-assisted synthesis increased the bandgap from 1.96 eV to 2.75 eV (**Figures 5b, c**), induced a phase transition from 2H-hexagonal to 3R-rhombohedral, and reduced the average crystallite size from 78.71 nm to 32.14 nm. Collectively, these changes suppressed electron-hole recombination and increased the density of surface-active sites, as evidenced by photoluminescence quenching. Under optimal conditions, the MoS_2-SDS NS achieved a degradation efficiency of 91.84%, significantly outperforming the 56.30% efficiency of bulk MoS_2 (**Figure 5d**). Mechanistic investigations using radical scavenging tests revealed that superoxide radicals (O_2^-) were the primary reactive species driving the degradation, while hydroxyl radicals (OH) and photogenerated h^+ played supporting roles (**Figure 5e**). Moreover, maintaining excellent chemical and structural stability over four consecutive cycles (**Figure 5f**), the photocatalyst demonstrated practical potential for wastewater treatment. **Figure 5g** has illustrated the mechanism of photocatalytic degradation of MB over the photocatalyst.

Likewise, Smriti et al. synthesized carbon-dot-modified hexagonal wurtzite CdS heterostructures (C-dots@CdS) containing 4, 6, and 8 wt% C-dots (designated as C-dots@CdS-4, -6, and -8) via a hydrothermal method and compared their performance with pristine CdS (104). The C-dots@CdS-6 composite (30 mg) achieved the highest photodegradation (97.32%) of Crystal Violet (CV)

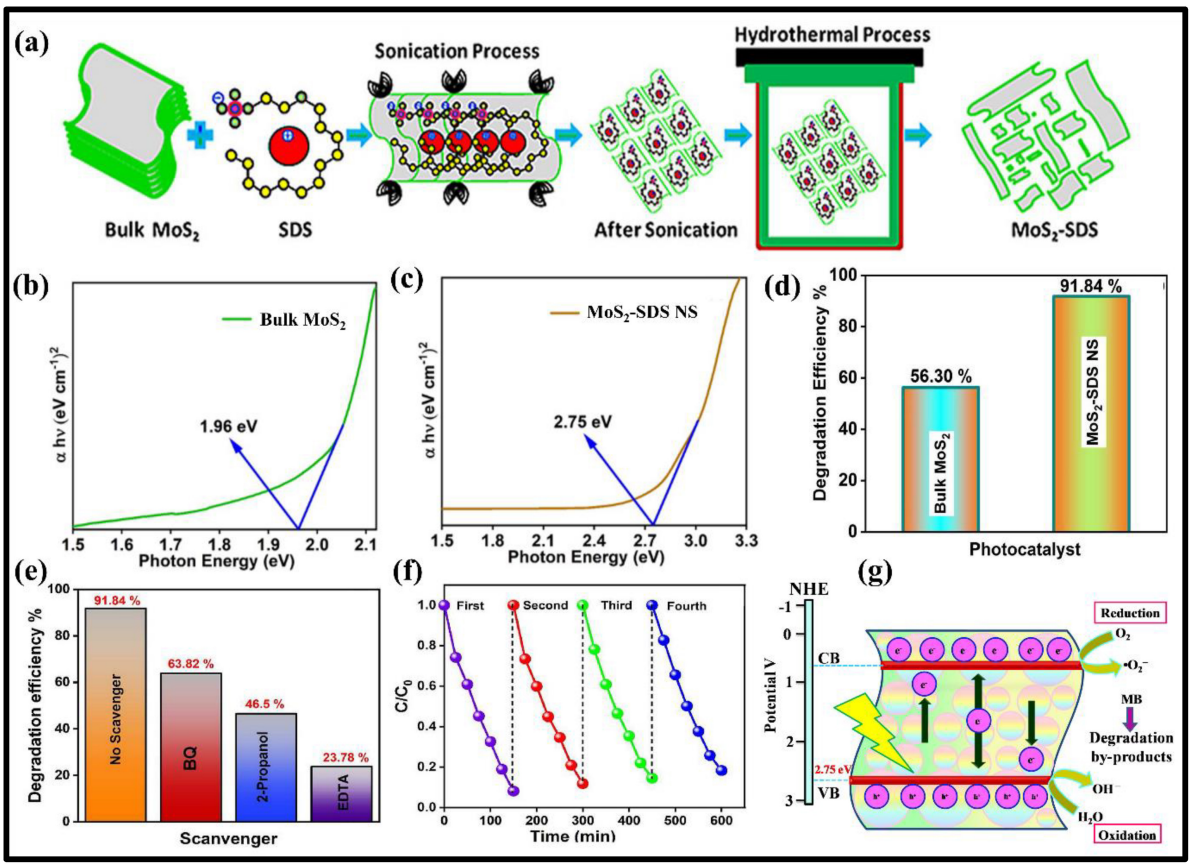


FIGURE 5 | (a) Graphical representation of MoS_2-SDS NS fabrication process, **(b, c)** bandgap of bulk MoS_2 and MoS_2-SDS NS, **(d)** comparison of photocatalytic degradation efficiency for MB dye, **(e)** degradation efficiency under the action of different scavengers, **(f)** recyclability, and **(g)** overall photocatalytic mechanism of MB degradation over MoS_2-SDS NS (103).

dye. Under neutral conditions, the negatively charged C-dots@CdS surface facilitated the adsorption of positively charged dye molecules. Increasing the dosage from 30 mg to 50 mg resulted in a significant decrease in activity due to photocatalyst agglomeration, which reduced light absorption capacity. In an acidic medium, efficiency declined due to proton-induced repulsion among pollutant molecules, whereas performance improved under basic conditions due to a higher concentration of hydroxyl radicals. The enhanced activity was attributed to the incorporation of C-dots, which increased surface area by mitigating agglomeration, improved light absorption, and promoted charge migration by suppressing recombination. The heterostructure maintained excellent chemical and structural stability over three consecutive cycles. In another study, Liu et al. fabricated an In_2S_3/2D Zr-MOF heterojunction via in-situ band-structure tuning and prepared composites M2, M5, and M8 with varying Zr-MOF contents (105). M5 demonstrated the best performance, degrading RR11 (5 h) and RB21 (13 h) dyes with efficiencies of 91.80% and 93.30%, respectively. This was attributed to the successful formation of a heterojunction that enhanced visible-light responsiveness, charge separation, and transfer while reducing interfacial resistance; additionally, M5 exhibited strong visible-light absorption. A significant reduction in the photoluminescence intensity of M5 compared to the pristine Zr-MOF, In2S3, M2, and M8 confirmed the suppression of charge-carrier recombination, while EIS and transient photocurrent measurements demonstrated rapid charge migration and separation. M5 also exhibited reliable reusability with good stability over at least four cycles. Scavenger experiments using methanol, $AgNO_3$, benzoquinone (BQ), and tert-butanol for h^+, e^-, O_2^-, and OH, respectively, revealed the most significant drop in performance (from 91.80% to 43.18%) with BQ, indicating the crucial role of O_2^- in the degradation of RR11. Although fading of the dye solution's color or a decrease in the UV-Vis absorbance peak does not constitute proof of complete degradation as this merely indicates the breakdown of specific chromophore groups (106). Complete mineralization (i.e., the conversion of the pollutant into CO_2 and H_2O) requires longer reaction times and a sufficiently strong redox potential from the photocatalyst. To confirm actual mineralization rather than just decolorization, the Total Organic Carbon (TOC) removal process using the 5% Zn-doped CuO-CdS nanocomposite was monitored under sunlight for 5 (106). The TOC removal rate was 18% for MB and 10% for Ciprofloxacin (CIP) within the

first 30 min. And this increased to 61% and 49% after 2 h, and finally reached 92% for MB and 76% for CIP after 5 h, with the degradation products being fully oxidized into CO_2 and H_2O. This comparison is revealing that although the catalyst achieved 98% decolorization of MB in 25 min, only 92% of the TOC was removed after 5 h, confirming that chromophore destruction and complete mineralization are distinct processes, with the latter serving as the rigorous benchmark for treatment performance. The lower TOC removal rate (76%) for CIP reflects its more stable core structure, highlighting that mineralization efficiency depends on the pollutant's structure and should be reported alongside the percentage of decolorization.

Antibiotic degradation

Rapid industrial development around the world has increased the number of pollutants in aquatic habitats, greatly affecting water quality despite the fact that water is essential for the survival of all living things (102). Antibiotics are widely used in the treatment of both humans and animals, making them important organic pollutants. But its widespread use has raised concerns about antibiotic resistance. The increased use of pharmaceuticals in human medicine, agriculture, and animal husbandry has resulted in water bodies becoming significantly polluted, making the water more poisonous (107). And due to the biotoxic and bioaccumulative properties of antibiotics and their resistance to degradation, it is essential to remove them from the environment as quickly as possible using effective and stable photocatalysts. In an investigation, Wang and team reported in situ sulfur vacancy modified In_2S_3 via employing the hydrothermal method (31). Utilizing L-cysteine as a sulfur source and reducing agent in different amounts resulted in the production of IS-2 (2.5 mmol), IS-3 (3.5 mmol), and IS-4 (4.5 mmol), respectively. The introduction of SVs in the photocatalyst promoted its photocatalytic performance. The composite IS-3 demonstrated superior photodegradation of the TC antibiotic with 83.6% efficiency within 1 h (**Figure 6a**). The optimized heterostructure IS-3 exhibited 4.62 and 1.74 times more rate constant and mineralization rate than pristine In_2S_3 (IS) (**Figure 6b**). However, the researchers further investigated TC removal in real water conditions comprised of different ions such as Cl^-, SO_4^{2-}, NO_3^- as demonstrated in **Figure 6c**. The experimental results confirmed reduction in performance from 83.6% to 75% and 75.6%, when NO_3^-, and Cl^- ions were added to the TC solution. The decreased activity was attributed to the hindered interaction of TC with catalytic sites of IS-3 due to enhanced electrostatic repulsion resulting from the addition of anionic ions. However, a major drop was noticed in the performance after addition of SO_4^{2-} ions which reacted with h^+s and transformed into SO_4^- and thereby reduced overall TC degradation efficacy. Moreover, reaction processes under different pH conditions revealed optimal performance under neutral conditions and basic conditions (**Figure 6d**). However, the acidic environment caused a major performance drop to 73.1%. The drop was due to the reduced production of O_2^- due to the reaction of O_2 with a proton producing OOH. Besides, researchers depicted two pathways of TC degradation using IS-3 photocatalyst. Both pathways resulted in the formation of non-harmful smaller molecules termed as P9, P10, P11, P12, P13, and P14, which ultimately converted into products such as H_2O and CO_2. The photoconversion of these highly toxic TC molecules into non-harmful products was verified by the T.E.S.T. software and the QSAR method. The study revealed the non-harmful nature of the photo-degradation products involving P8, P9, P10, and P13 and also exhibited a lower bioconcentration factor as compared to TC. Therefore, all these studies and results proved the successful degradation of toxic TC pollutants into final smaller, non-toxic substances as the photocatalytic process continued. Moreover, **Figure 6e** represents the overall phot-driven degradation mechanism of the TC using the IS-3 photocatalyst. The photocatalytic reactions involved in the process are provided below as follows:

$$\text{IS-3} + hv \rightarrow e^- + h^+$$
$$e^- + O_2 \rightarrow \cdot O_2^-$$
$$\text{TC} + \cdot O_2^-/h^+ \rightarrow \text{Degradation products}$$

The mechanism involved the generation of e^-–h^+ pairs by the photocatalyst under light illumination, which were further transferred to the photocatalyst's surface for the redox reactions. However, some of these electrons are trapped by an induced sulfur vacancy in the photocatalyst, which acts as e^- trapping center. Therefore, it ensured effective separation and efficient migration of the photogenerated charge carriers with suppressed recombination. Also, the better charge separation facilitated the effective interaction of e^-s with the adsorbed O_2 molecules to produce O_2^- radical. And these ROS further reacted with pollutant molecule, and degraded them into simpler ones.

In another report, a Z-scheme CdS/Bi_3O_4Cl heterostructure was synthesized by coupling CdS nanospheres and BiOCl NSs via a surfactant-free hydrothermal method (108). The optimized CdS/Bi_3O_4Cl-50 composite demonstrated enhanced visible-light-driven degradation of TC and CIP. It achieved 84.2% CIP degradation within 120 min with an apparent rate constant of 0.0151 min^{-1} values, 10.63 and 1.97 times higher than those of pristine Bi_3O_4Cl and CdS, respectively; the TC rate constant (0.0643 min^{-1}) was 2.14 and 4.34 times higher. This performance was attributed to three synergistic factors. First, the staggered band alignment between CdS (ECB = −0.50 eV) and Bi_3O_4Cl (ECB = 0.55 eV) established a direct Z-scheme charge transfer channel, maintaining strong redox potential while achieving efficient charge separation,

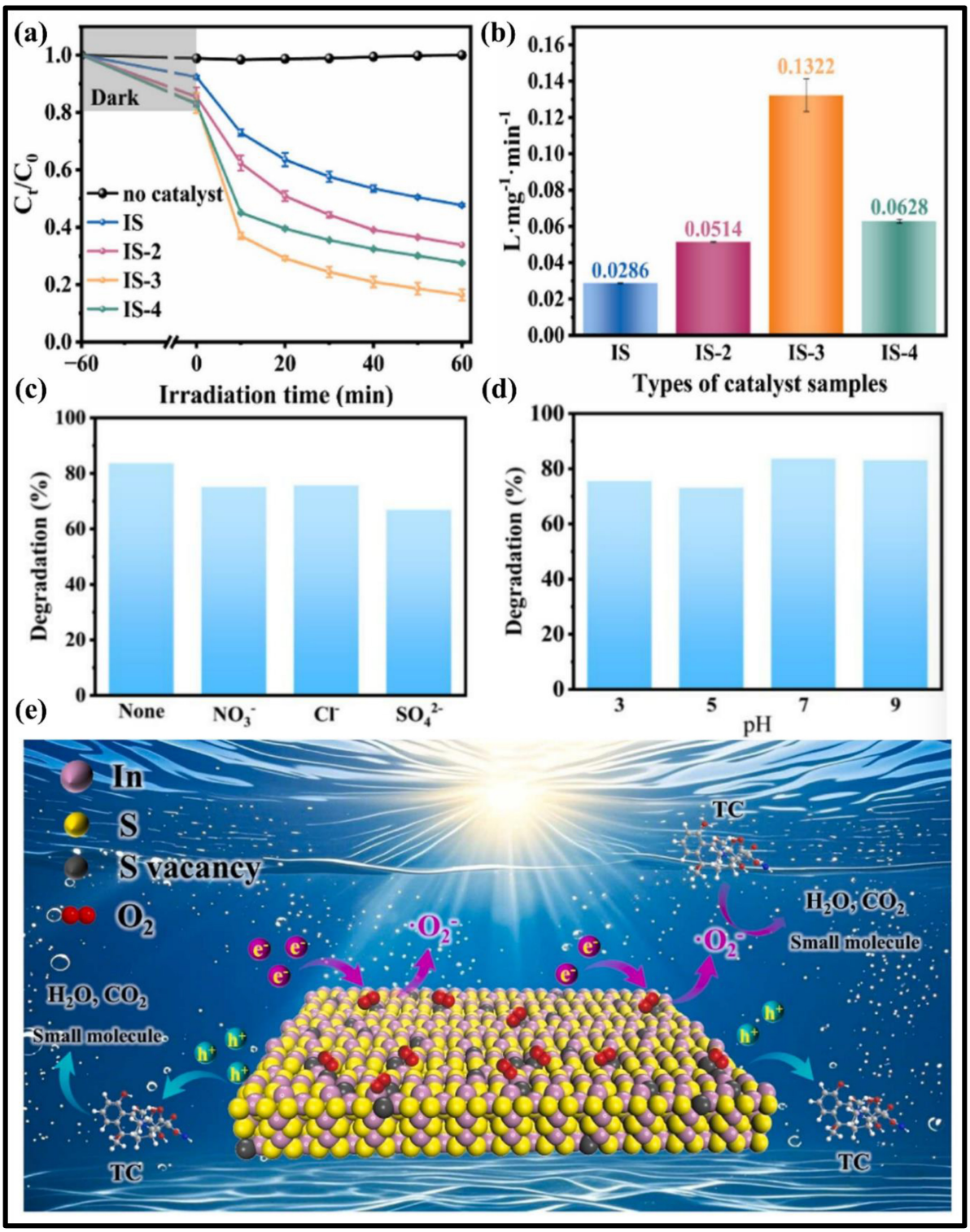


FIGURE 6 | (a, b) Photocatalytic TC degradation efficiency and rate constant using different photocatalysts, respectively; **(c, d)** effect of anions and pH over the photocatalytic performance, respectively; **(e)** graphical representation of overall mechanism of TC photo-degradation (31).

as confirmed by electrochemical impedance spectroscopy and transient photocurrent measurements. Second, electron spin resonance and radical trapping experiments confirmed the abundant generation of superoxide (O_2^-) and hydroxyl (OH) radicals, which facilitate oxidative degradation. Third, the composite exhibited a high surface area (42.902 $m^2\ g^{-1}$) and mesopores (~20 nm), providing abundant active sites. HPLC-MS analysis revealed the formation of CO_2 and H_2O via stepwise ring-opening mineralization, with TOC removal efficiencies of 54.86% (CIP) and 63.88% (TC). Moreover, the

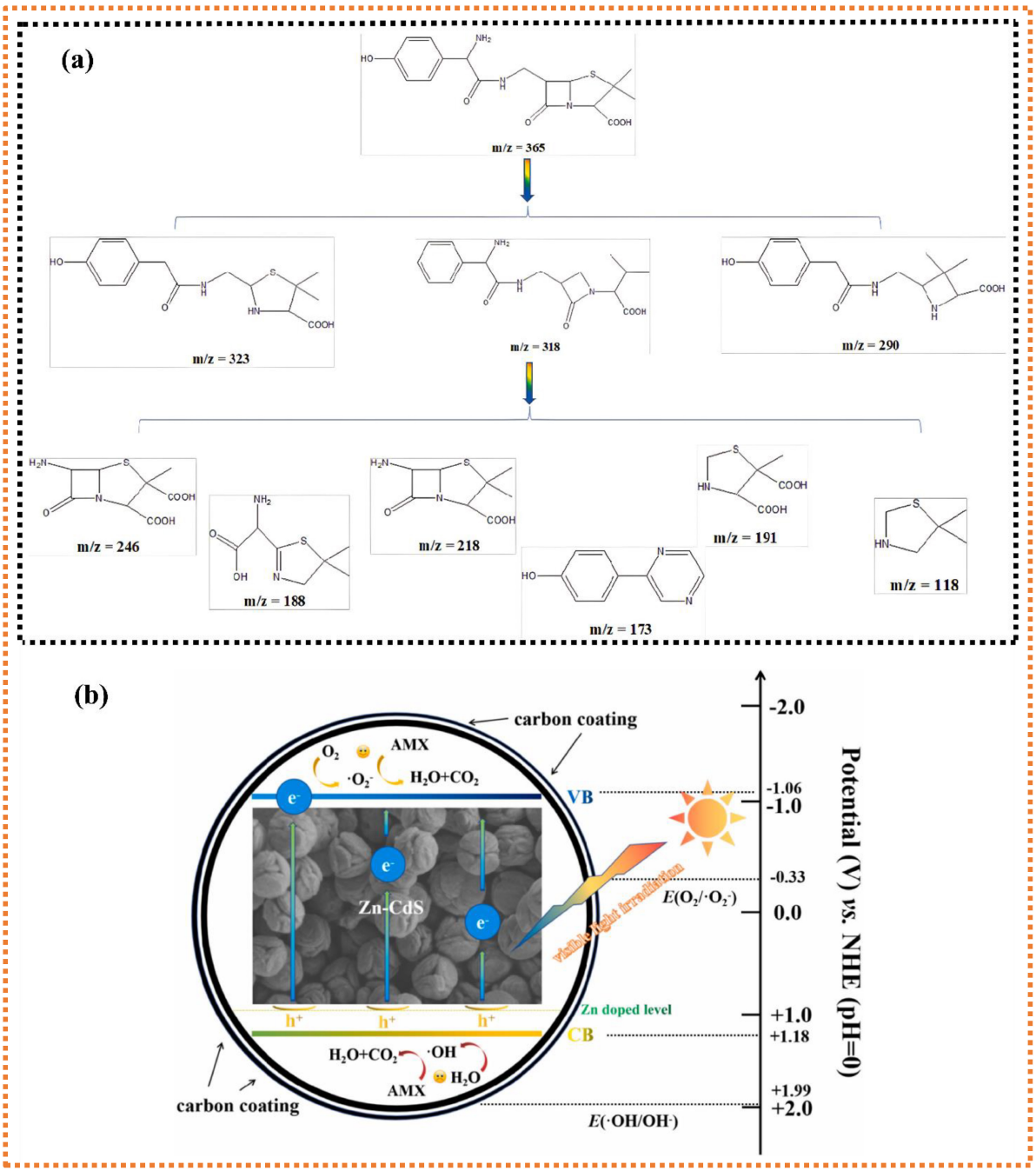


FIGURE 7 | (a) Proposed AMX degradation pathway via HPLC-MS analysis, **(b)** Schematic representation of AMX photodegradation mechanism over 2% Zn-CdS@C (109).

photocatalyst remained stable for three consecutive cycles without undergoing any phase or structural changes.

Likewise, Liu et al. synthesized a carbon-coated, Zn-doped CdS core-shell photocatalyst (Zn-CdS@C) via a one-pot solvothermal method for the photodegradation of amoxicillin (AMX) (109). Pristine CdS exhibited poor photocatalytic activity with a rate constant of 0.0055 min^{-1}, primarily due to the rapid recombination of photogenerated e^{-}–h^{+} pairs. Carbon coating slightly enhanced the activity, resulting in a rate constant of 0.0089 min^{-1}, whereas the optimized 2% Zn-CdS@C sample achieved a significantly higher value of 0.0441 min^{-1}. This improvement was attributed to the synergistic effect of Zn^{2+} doping and carbon coating. Zn^{2+} ions substituted for Cd^{2+} in the CdS lattice, creating electron-accepting sites and extending the charge-carrier lifetime. Meanwhile, the carbon shell enhanced electrical conductivity, facilitated interfacial charge transfer, and protected CdS against photocorrosion. Photoluminescence and time-resolved photoluminescence measurements

TABLE 1 | Summary of representative metal sulfide-based photocatalysts for wastewater remediation: comparative analysis of structural modifications, operational parameters, pollutant degradation, TOC mineralization efficiency, cyclic durability, and metal-ion leaching.

Photocatalyst	Modification strategy	Target pollutant	Initial conc. (C_0)	Catalyst dosage	Light source	Time (min)	Removal efficiency (%)	TOC removal (%)	Cycles	Metal leaching	Refs.
g-CN/CdS	Heterojunction	Congo Red (CR)	20 mg/L	0.5 g/L	300 W xenon lamp	120	99.85%	5%	–	–	(111)
$NaFeS_2$	Novel material	Methylene blue (MB) Indigo carmine (IC)	20 ppm of 250 mL aqueous solution of MB/IC	0.060 g	125 W mercury vapor lamp	105 min 45 min	97% 99%	82% removal at 105 min. 84% removal at 105 min.	Three cycles	–	(112)
BGO-CuS	Heterojunction	MB	15 ppm	20 mg/100 mL	Visible light	60 min	95%	Decrease upto 86% under sunlight irradiation	Five cycles	Less than 1% loss of Cu ions (0.1 mg on average per reusability trial)	(113)
ZIS/BTO-40	S-scheme heterojunction	Tetracycline (TC)	20 ppm, 50 mL	10 mg	300 W Xenon lamp	60 min	82.1%	–	Four cycles	–	(100)
$Fe_3O_4/BiVO_4$/CdS (FBC-3)	Ternary Z-scheme Heterojunction	TC	10 mg/L	100 mg	300 W Xenon lamp	90 min	87.37%	Removal rate reaches 41.3%	Five cycles	Fe = 2.130 (mg/L) Bi = 0.010 (mg/L) Cd = 5.980 (mg/L)	(114)
GO/CdS	Heterostructure formation	TC	20 mg/L	10 mg	350 W Xenon lamp	60 min	95%	74.92% within 60 min	Three cycles	Released Cd^{2+} concentration range 1.816×10^{-8}–2.508×10^{-8} g/L	(115)
La-Bi_2WO_6/CdS (LBC-40)	Direct Z-scheme	OTC	20 mg/L	1.0 g/L	65 W energy-saving lamp	120 min	85.28%	–	Four cycles	–	(116)
CoS_2/CdS	Co-catalyst loading	TC	30 mg/L	30 mg	18 W LED lamp	80 min	Near to 100%	45.9% after 10 h	90% TC degradation rate even after six cycles	No obvious leaching during recycling process	(117)
MIL-101 (Fe)/CdS (MC-3)	S-scheme heterojunction (synergistic photocatalysis-Fenton conditions)	Tetracycline hydrochloride (TCH)	10 mg/L	0.4 g/L	1500 mW LED lamp	24 min	96%	82.9% under 24 min	Eight cycles	<0.1 mg/L For both Cd and Fe elements	(118)
Bi_2WO_6/ZnO/CdS (WZC-25)	Double Z-scheme	Rhodamine B (RhB) Norfloxacin (NOR)	5 mg/L	50 mg	300 W Xenon lamp	25 min 80 min	98.8% 96.9%	Above 50%	Four cycles	–	(119)

confirmed reduced charge recombination and accelerated charge transfer. Radical-scavenging experiments using IPA, TEOA, and BQ revealed that O_2^- was the primary reactive species responsible for AMX degradation. Intermediates formed during AMX photodegradation were analyzed using HPLC-MS, and the degradation pathway is illustrated in **Figure 7a**. Subsequently, ring-opening and oxidation reactions occurred, wherein the resulting intermediates gradually transformed into smaller molecules and ultimately mineralized into H_2O and CO_2. Additionally, TOC analysis was performed to evaluate degradation efficiency by monitoring complex degradation products; the 2% Zn-CdS@C sample exhibited the best performance after 3 h of illumination, achieving a TOC removal efficiency of 64.53%. Cycling experiments revealed no significant decline in photocatalytic activity, and the phase structure remained intact even after five cycles, indicating that the carbon shell effectively protected the sulfide photocatalyst from photocorrosion. The proposed photodegradation mechanism of AMX has been illustrated in **Figure 7b**, as proposed by the researchers in the study.

Both natural waters and wastewaters contain various inorganic anions that interact differently with charge carriers and ROS, thereby influencing the overall rate of photocatalytic reactions (37, 110). However, most studies on metal sulfide photocatalysts rely on model pollutant solutions prepared in DIW, failing to capture the compositional complexity of real wastewater. Actual municipal and industrial wastewaters contain naturally occurring inorganic ions such as chloride, nitrate, sulfate, bicarbonate, and phosphate, alongside dissolved organic matter and suspended solids, all of which can affect photocatalytic degradation. Balakrishnan et al. systematically investigated these matrix effects while degrading sulfamethoxazole (SMX) via peroxymonosulfate (PMS) activation using a reusable double Z-scheme ternary hydrogel (37). They achieved 99% removal of SMX (10 mg/L) under visible light within 20 min, with a rate constant of 0.191 min^{-1}. To examine the matrix effects, they first assessed the impact of co-ions (50 mg/L) commonly found in real wastewater, including chloride, nitrate, sulfate, bicarbonate, and phosphate. The order of degradation efficiency was as follows: Control (99%) > Sulfate (94%) > Nitrate (88%) > Phosphate (80%) > Chloride (67%) > Bicarbonate (66%). Bicarbonate converted sulfate and hydroxyl radicals into less reactive carbonate species, phosphate deactivated the catalyst's active sites, and chloride generated Cl_2^- radicals with lower oxidizing potential. Subsequently, the system was tested using distilled, tap, and lake water; a lower SMX removal rate was observed only with lake water, attributed to higher turbidity, ion concentrations, and impurities. Finally, real industrial wastewater from Odisha, India, was treated, achieving a maximum COD removal of 61%. Scavenger studies revealed that electrons and sulfate radicals played the primary role, while superoxide and hydroxyl radicals played a secondary role. The hydrogel retained 87% of its activity over 10 cycles, and a dual-reactor continuous-flow setup increased SMX degradation from 64% to 83%. Similarly, Das et al. developed a lightweight and highly porous MoS_2/graphene aerogel for the degradation of TC (110). Upon exposure to visible light for 120 min, 97% of TC was removed at a concentration of 5 mg/L and 80% at 25 mg/L. Large mesopores enhanced light penetration, mass transfer, and charge separation, resulting in photocatalytic capacity and rates approximately 1.6 and 3.1 times higher, respectively, than those of conventional aerogels. To assess practical applicability, TC degradation rates were compared across DIW, municipal wastewater (MWW), and hospital wastewater (HWW); a reduction of 9.5% was observed in MWW and 15.7% in HWW. The reasons for this reduction included: complex formation between TC and co-existing organic substances; competition for adsorption and catalytic sites; a decrease in holes and OH radicals due to high bicarbonate levels; and reduced light penetration caused by turbidity. Among the four anions tested (Cl^-, NO_3^-, SO_4^{2-}, HCO_3^-), bicarbonate caused the greatest inhibition of TC removal, while the others caused moderate inhibition. Mechanistic studies (using scavengers and EPR) revealed that singlet oxygen ($^1O_2$) and photogenerated holes played the primary roles in TC degradation, whereas superoxide and OH radicals played secondary roles. After 120 min, 67% of TOC was removed; the aerogel remained structurally and morphologically stable for three cycles; and a resazurin-based toxicity test confirmed that the final products were less harmful than TC. Despite matrix-related limitations, an average of approximately 84.4% of TC was removed from real wastewater. Moreover, **Table 1** presents a comparative overview of specific metal sulfide photocatalysts. It includes key parameters such as catalyst dosage, operating wavelength, pollutant degradation rate, and the rate of TOC mineralization. Additionally, the table provides data on cyclic durability and post-reaction metal-ion leaching, offering insights into the structural stability and environmental impact (eco-toxicological sustainability) of each modified system during repeated use.

Conclusion

Metal sulfide SC photocatalysis is one of the most promising emerging technologies for the reduction of environmental pollution and protection of ecosystems. This study systematically explained the special properties of metal sulfides, particularly their ability to change their narrow band gaps and high visible-light absorption and use them as important possibilities for effective contamination degradation. However, there are significant problems with pristine metal sulfides, such as severe photocorrosion and fast photogenerated charge carrier recombination. However, the limitations have been overcome to a large extent by the application of sophisticated synthesis control and

modification techniques such as precise control of vacancies, doping, and heterojunction construction. In order to predict the transport, adsorption, and redox chemistry of target contaminants, it is essential to understand the structure-function relationship at surface active sites. The challenges in this technology that must be addressed include the durability of the photocatalysts and their ability to be produced on a large scale at low cost, as well as to function in complex wastewater systems in real-world applications. Multidisciplinary research and development efforts that are systematic and thorough, starting from potential breakthroughs at the laboratory scale, can bring metal sulfide photocatalysts to fruition for sustainable environmental remediation at scale.

Conflict of interest

The authors declare that the research was conducted in the absence of any commercial or financial relationships that could be construed as a potential conflict of interest.

References

1. Solangi NH, Karri RR, Mazari SA, Mubarak NM, Jatoi AS, Malafaia G, et al. MXene as emerging material for photocatalytic degradation of environmental pollutants. *Coord Chem Rev*. (2023) 477:214965.
2. Ahmad K, Ghatak HR, Ahuja S. A review on photocatalytic remediation of environmental pollutants and H_2 production through water splitting: a sustainable approach. *Environ Technol Innov*. (2020) 19:100893.
3. Vieira Y, Netto MS, Lima ÉC, Anastopoulos I, Oliveira ML, Dotto GL. An overview of geological originated materials as a trend for adsorption in wastewater treatment. *Geosci Front*. (2022) 13:101150.
4. Ahmad A. Using of activated carbon adsorption in wastewater industries. *J Chem Lett*. (2022) 3:2–9.
5. Benalia MC, Youcef L, Bouaziz MG, Achour S, Menasra H. Removal of heavy metals from industrial wastewater by chemical precipitation: mechanisms and sludge characterization. *Arab J Sci Eng*. (2022) 47:5587–99.
6. Liang G, Li S, Yu X, Bu Q, Qu H, Zhu H, et al. Black carbon-mediated degradation of organic pollutants: a critical review. *Process Saf Environ Prot*. (2022) 160:610–9.
7. Doukani K, Boukirat D, Boumezrag A, Bouhenni H, Bounouira Y. Biodegradation of pollutants. In: Ali GAM, Makhlouf SHA editors. *Handbook of Biodegradable Materials*. Cham: Springer (2022). p. 1–27.
8. Sun P, Jing D, Durham DB, Sapkota B, Chen Y, Anderson JL. Ion-specific precipitation of extractants enables rare-earth separation and wastewater remediation from solvent extraction of critical elements. *Environ Sci Technol*. (2026) 60:6239–48.
9. Padinhattath SP, Shaibuna M, Gardas RL. Solvent extraction with hydrophobic deep eutectic solvents: a benign alternative for efficient industrial wastewater treatment. In: *Deep Eutectic Solvents*. Washington (DC): ACS Publications (2025). p. 271–90.
10. Huang L, Cui X, Dang H, Huang Y, Li Q, Ran T, et al. Urea interfacial polymerization-based ultra-permeable polyamide composite membrane for efficient piggery wastewater purification. *Chem Eng J*. (2025) 503:158376.
11. Zhang S, Zhang X, Shen X, Lu X, Guo Y, Li Y, et al. Research status of membrane separation technology in the treatment of antibiotic wastewater. *Environ Sci Water Res Technol*. (2025) 11:1386–400.
12. Hou T, Zhou Y, Zhao Y, Li J, Zhou L. Removal of p-nitrophenol in high-salinity wastewater by chlorine-mediated electrochemical advanced oxidation. *Sep Purif Technol*. (2025) 378:134532.
13. Shamshad J, Rehman RU. Innovative approaches to sustainable wastewater treatment: a comprehensive exploration of conventional and emerging technologies. *Environ Sci Adv*. (2025) 4:189–222.
14. Wang W, Shao T, Cui Z, Gao F, Tai Y, Liu Q. Modulating oxygen vacancies over Bi_2O_3 by CeO_2 and acid etching boosts synergistic photocatalytic ozonation towards quinoline contaminants removal. *Chem Eng J*. (2025) 520:166204.
15. Wen Q, An X, Huang B, Zhang J, He CS, Zou J, et al. Catalytic ozonation for hospital wastewater treatment: challenge of simultaneous removal of pharmaceutical contaminants and pathogenic microorganisms. *Chem Eng J*. (2025) 515:163644.
16. Rukhsar A, Iqbal ZF, Khan MS, Zainab SA, Nawaz S, Kim TH, et al. Chitosan-based adsorbents and catalysts for removal of toxic pollutants from water and wastewater. *Top Catal*. (2025) 68:893–915.
17. Kakavandi B, Dehghanifard E, Bashardoust P, Ahmadi M, Sanei E, Malekpoor M. Effectiveness of sono-photo-Fenton processes for removal of emerging contaminants from water and wastewater. In: Dehghani MH, Khan NA editors. *Ultrasonic Treatment of Water and Wastewater*. Elsevier (2026). p. 307–28.
18. Sahmi A, Berkani G, Lahmar H, Benamira M, Aksas H, Trari M. Advancements in sono-photo-electrocatalytic oxidation for the removal of toxic contaminants in wastewaters. *Int J Environ Sci Technol*. (2026) 23:132.
19. Singh A, Sinha MK, Khuntia S. Mechanistic evidence of hydroxyl radical prevalence in sulfate-radical-oriented advanced oxidation processes. *Langmuir*. (2025) 41:31433–43.
20. Bączkowska E, Pierpaoli M, Gamoń F, Luczkiewicz A, Fudala-Ksiazek S, Bray R, et al. On-site medical wastewater treatment enabling sustainable water reclamation: merged advanced oxidation process for disinfection, toxicity, and contaminants removal. *J Water Process Eng*. (2025) 72:107562.
21. Aziz KHH, Mustafa FS, Karim MA, Hama S. Pharmaceutical pollution in the aquatic environment: advanced oxidation processes as efficient treatment approaches: a review. *Mater Adv*. (2025) 6:3433–54.
22. Lee SY, Park SJ. TiO_2 photocatalyst for water treatment applications. *J Ind Eng Chem*. (2013) 19:1761–9.
23. Belver C, Bedia J, Gómez-Avilés A, Peñas-Garzón M, Rodriguez JJ. Semiconductor photocatalysis for water purification. In: Thomas S, Pasquini D, Leu SY, Gopakumar DA editors. *Nanoscale Materials in Water Purification*. Amsterdam: Elsevier (2019). p. 581–651.
24. Xu Y, Chiam SL, Leo CP, Hu Z. Recent advances in photocatalytic TiO_2-based membranes for eliminating water pollutants. *Sep Purif Rev*. (2026) 55:150–67.
25. Roushree R, Haimbodi R. Recent advances in ZnO-based nanocomposites for amoxicillin photocatalytic degradation and adsorption in wastewater: a review. *J Inorg Organomet Polym Mater*. (2026) 36:26–63.
26. Liaqat M, Younas A, Iqbal T, Afsheen S, Zubair M, Kamran SKS, et al. Synthesis and characterization of ZnO/$BiVO_4$ nanocomposites as heterogeneous photocatalysts for antimicrobial activities and waste water treatment. *Mater Chem Phys*. (2024) 315:128923.
27. Zhong S, Wang Y, Chen Y, Jiang X, Lin M, Lin C, et al. Improved piezo-photocatalysis for aquatic multi-pollutant removal via BiOBr/$BaTiO_3$ heterojunction construction. *Chem Eng J*. (2024) 488:151002.
28. Hao H, Lang X. Metal sulfide photocatalysis: visible-light-induced organic transformations. *ChemCatChem*. (2019) 11:1378–93.
29. Cheng L, Xiang Q, Liao Y, Zhang H. CdS-based photocatalysts. *Energy Environ Sci*. (2018) 11:1362–91.

30. Abbasi M, Rafique U, Murtaza G, Ashraf MA. Synthesis, characterisation and photocatalytic performance of ZnS coupled Ag_2S nanoparticles: a remediation model for environmental pollutants. *Arab J Chem*. (2018) 11:827–37.
31. Wang S, Ren H, Zeng L, Lohwacharin J, Huang Y, Wang C. Sulfur vacancies for enhanced photocatalytic molecular oxygen activation and antibiotic degradation over In_2S_3. *J Environ Chem Eng*. (2025) 13:119134.
32. Panchal D, Sharma A, Pal S. Engineered MoS_2 nanostructures for improved photocatalytic applications in water treatment. *Mater Today Sustain*. (2023) 21:100264.
33. Gao Q, Zheng X, Lin J, Zhai J, Yang F, Chen X, et al. Design concept of metal sulfide photocatalyst for efficient photocatalytic hydrogen evolution. *Nano-Micro Lett*. (2026) 18:266.
34. Tahir MB, Rafique M, Rafique MS, Fatima N, Israr Z. Metal oxide- and metal sulfide-based nanomaterials as photocatalysts. In: Tahir MB, Rafique M, Rafique MS editors. *Nanotechnology and Photocatalysis for Environmental Applications*. Amsterdam: Elsevier (2020). p. 77–96.
35. Arif M. Photocatalytic degradation of dyes by metal sulfide-chitosan based composites: a comprehensive review. *RSC Adv*. (2026) 16:5353–73.
36. Shivaji K, Sridharan K, Kirubakaran DD, Velusamy J, Emadian SS, Krishnamurthy S, et al. Biofunctionalized CdS quantum dots: a case study on nanomaterial toxicity in the photocatalytic wastewater treatment process. *ACS Omega*. (2023) 8:19413.
37. Tripathy H, Balakrishnan A, Chinthala M, Kumar A. Ternary indium sulfide based 3D hydrogels as versatile photocatalysts: unraveling peroxymonosulfate activation for sulfamethoxazole degradation and H_2O_2 production. *Ind Eng Chem Res*. (2024) 63:20125–43.
38. Li K, Chen J, Bai S, Wen X, Song S, Yu Q, et al. Intracellular oxidative stress and cadmium ions release induce cytotoxicity of unmodified cadmium sulfide quantum dots. *Toxicol In Vitro*. (2009) 23:1007–13.
39. Liu H, Gao H, Long M, Fu H, Alvarez PJ, Li Q, et al. Sunlight promotes fast release of hazardous cadmium from widely-used commercial cadmium pigment. *Environ Sci Technol*. (2017) 51:6877–86.
40. Wang M, Cai L, Wang Y, Zhou F, Xu K, Tao X, et al. Graphene-draped semiconductors for enhanced photocorrosion resistance and photocatalytic properties. *J Am Chem Soc*. (2017) 139:4144–51.
41. Li S, Zhang T, Zheng H, Niu J, Zhang W, Ma J, et al. Efficient photo-Fenton degradation of water pollutants via peracetic acid activation over sulfur vacancies-rich metal sulfides/MXenes. *Appl Catal B Environ Energy*. (2025) 366:125000.
42. She H, Sun Y, Li S, Huang J, Wang L, Zhu G, et al. Synthesis of non-noble metal nickel doped sulfide solid solution for improved photocatalytic performance. *Appl Catal B Environ*. (2019) 245:439–47.
43. Liu Y, Wang H, Yuan X, Wu Y, Wang H, Tan YZ, et al. Roles of sulfur-edge sites, metal-edge sites, terrace sites, and defects in metal sulfides for photocatalysis. *Chem Catal*. (2021) 1:44–68.
44. Liu Y, Zheng X, Yang Y, Li J, Liu W, Shen Y, et al. Photocatalytic hydrogen evolution using ternary-metal-sulfide/TiO_2 heterojunction photocatalysts. *ChemCatChem*. (2022) 14:e202101439.
45. Song Z, Liu Y, Zhang B, Song S, Zhou Z, Huang Y, et al. Magnetic grinding synthesis of copper sulfide-based photocatalytic composites for the degradation of organic dyes under visible light. *New J Chem*. (2023) 47:2286–95.
46. Gadore V, Mishra SR, Ahmaruzzaman M. Metal sulphides and their heterojunctions for photocatalytic degradation of organic dyes—a comprehensive review. *Environ Sci Pollut Res Int*. (2023) 30:90410–57.
47. Zhu Q, Xu Q, Du M, Zeng X, Zhong G, Qiu B, et al. Recent progress of metal sulfide photocatalysts for solar energy conversion. *Adv Mater*. (2022) 34:2202929.
48. Frame FA, Osterloh FE. CdSe-MoS_2: a quantum size-confined photocatalyst for hydrogen evolution from water under visible light. *J Phys Chem C*. (2010) 114:10628–33.
49. Shen R, Ren D, Ding Y, Guan Y, Ng YH, Zhang P, et al. Nanostructured CdS for efficient photocatalytic H_2 evolution: a review. *Sci China Mater*. (2020) 63:2153–88.
50. Zhang J, Wageh S, Al-Ghamdi A, Yu J. New understanding on the different photocatalytic activity of wurtzite and zinc-blende CdS. *Appl Catal B Environ*. (2016) 192:101–7.
51. Li K, Han M, Chen R, Li SL, Xie SL, Mao C, et al. Hexagonal@cubic CdS core@shell nanorod photocatalyst for highly active production of H_2 with unprecedented stability. *Adv Mater*. (2016) 28:8906–11.
52. Zelati A, Taghavimendi R, Bakhshayeshi A. First-principles investigation of optoelectronic properties of novel SnS_2 with a cubic structure. *Solid State Commun*. (2021) 333:114344.
53. Zhang J, Huang G, Zeng J, Jiang X, Shi Y, Lin S, et al. SnS_2 nanosheets coupled with 2D ultrathin MoS_2 nanolayers as face-to-face 2D/2D heterojunction photocatalysts with excellent photocatalytic and photoelectrochemical activities. *J Alloys Compd*. (2019) 775:726–35.
54. Shen S, Guo P, Zhao L, Du Y, Guo L. Insights into photoluminescence property and photocatalytic activity of cubic and rhombohedral $ZnIn_2S_4$. *J Solid State Chem*. (2011) 184:2250–6. doi: 10.1016/j.jssc.2011.06.033
55. Wang J, Sun S, Zhou R, Li Y, He Z, Ding H, et al. A review: synthesis, modification and photocatalytic applications of $ZnIn_2S_4$. *J Mater Sci Technol*. (2021) 78:1–19.
56. Kumar Y, Kumar R, Raizada P, Khan AAP, Van Le Q, Singh P, et al. Novel Z-scheme $ZnIn_2S_4$-based photocatalysts for solar-driven environmental and energy applications: progress and perspectives. *J Mater Sci Technol*. (2021) 87:234–57.
57. Hou Z, Li Y, Liu J, Shen H, Huo X. The visible light-driven highly efficient photocatalytic properties of Cu_2ZnSnS_4 nanoparticles synthesized by a hydrothermal method. *New J Chem*. (2021) 45:1743–52.
58. Weng B, Qi MY, Han C, Tang ZR, Xu YJ. Photocorrosion inhibition of semiconductor-based photocatalysts: basic principle, current development, and future perspective. *ACS Catal*. (2019) 9:4642–87.
59. Gholipour MR, Dinh CT, Béland F, Do TO. Nanocomposite heterojunctions as sunlight-driven photocatalysts for hydrogen production from water splitting. *Nanoscale*. (2015) 7:8187–208.
60. Liu Z, Tang C, Yu Z, Li S, Deng C, Liu S, et al. Photocorrosion suppression of copper sulfide via hybridization with amino-functionalized metal-organic framework for natural sunlight-driven photocatalysis. *Fuel*. (2024) 376:132721.
61. Yi L, Qiu J, Xie Z, Chen Y, Xie Y, Wang Y, et al. Preparation of Z-type NiO/Ag/CdS heterojunction photocatalyst and its photocatalytic hydrogen production performance. *J Photochem Photobiol A Chem*. (2026) 482:117533.
62. Sur S, Öztürk Z, Öztaş M, Bedir M. Deposition and characterization of polycrystalline ZnS films prepared using a chemical bath deposition technique in an aqueous/ethanolic solution. *Phys Scr*. (2010) 82:045604.
63. Peng K, Wang H, Li X, Wang J, Xu L, Gao H, et al. One-step hydrothermal growth of MoS_2 nanosheets/CdS nanoparticles heterostructures on montmorillonite for enhanced visible light photocatalytic activity. *Appl Clay Sci*. (2019) 175:86–93.
64. Mulu M, RamaDevi D, Belachew N, Basavaiah K. Hydrothermal green synthesis of MoS_2 nanosheets for pollution abatement and antifungal applications. *RSC Adv*. (2021) 11:24536–42.
65. Singh A, Ahmed A, Sharma A, Sharma C, Paul S, Khosla A, et al. Promising photocatalytic degradation of methyl orange dye via sol-gel synthesized Ag-CdS@Pr-TiO_2 core/shell nanoparticles. *Phys B Condens Matter*. (2021) 616:413121.
66. Sankar M, Jothibas M, Muthuvel A, Rajeshwari A, Jeyakumar SJ. Structural, optical and photocatalytic degradation of organic dyes by sol-gel prepared Ni-doped CdS nanoparticles. *Surf Interfaces*. (2020) 21:100775.

67. Wang K, Tang F, Yao XZ, Hitanshu K, Gan L. Chemical vapor deposition of two-dimensional transition metal sulfides on carbon paper for electrocatalytic hydrogen evolution. *New Carbon Mater*. (2022) 37:1183–91.
68. Carlsson JO, Martin PM. Chemical vapor deposition. In: Martin PM editor. *Handbook of Deposition Technologies for Films and Coatings*. Oxford: Elsevier (2010). p. 314–63.
69. Fu Y, Li Q, Liu J, Jiao Y, Hu S, Wang H, et al. In-situ chemical vapor deposition to fabricate cuprous oxide/copper sulfide core-shell flowers with boosted and stable wide-spectral region photocatalytic performance. *J Colloid Interface Sci*. (2020) 570:143–52.
70. Buckingham MA, Catherall AL, Hill MS, Johnson AL, Parish JD. Aerosol-assisted chemical vapor deposition of CdS from xanthate single source precursors. *Cryst Growth Des*. (2017) 17:907–12.
71. Ren H, Labidi A, Chang T, Miao Z, Feng X, Wang C. Coordination engineering in dual S-scheme heterojunction for photocatalytic applications: research progress, key challenges and future horizons. *Coord Chem Rev*. (2026) 548:217183.
72. Li W, Zuo G, Ma S, Xi L, Ouyang C, He M, et al. Localized photothermal effect mediated hollow S-scheme $NiCo_2O_4$@$ZnIn_2S_4$ for enhanced photocatalytic hydrogen evolution. *Appl Catal B Environ Energy*. (2025) 365:124971.
73. Wu Z, Liu J, Zhen L, Shi J, Deng H. Enhanced degradation of ciprofloxacin via Co-doped $Bi_2Fe_4O_9$ photocatalysis under peroxydisulfate activation. *Green Energy Environ*. (2025) 10:1311–25.
74. Gao Q, Wang T, Ni L, Li Z, Du X, Rong S, et al. Constructing S-scheme 3D $Zn_3In_2S_6$/ReS_2 heterojunction photocatalyst for simultaneous organic pollutants degradation and hydrogen production. *Green Energy Environ*. (2025) 10(10):2071–85.
75. Salazar-Marín D, Oza G, Real JD, Cervantes-Uribe A, Pérez-Vidal H, Kesarla M, et al. Distinguishing between type II and S-scheme heterojunction materials: a comprehensive review. *Appl Surf Sci Adv*. (2024) 19:100536.
76. Bard AJ. Photoelectrochemistry and heterogeneous photo-catalysis at semiconductors. *J Photochem*. (1979) 10:59–75.
77. Sharma P, Rana S, Dhiman P, Naushad M, Wang T, Mola GT, et al. Recent advances in rare earth metal oxides and sulfides-based heterojunctions for photocatalytic energy applications. *J Rare Earths*. (2026) (in press).
78. Li L, Li L, Sun T, Yu X, Long L, Xu L, et al. Novel $H_3PW_{12}O_{40}$/TiO_2-g-C_3N_4 type-II heterojunction photocatalyst with enhanced visible-light photocatalytic properties. *J Solid State Chem*. (2019) 274:152–61.
79. Chang CJ, Kao YC, Lin KS, Chen CY, Kang CW, Yang TH. Carbon fiber cloth@BiOBr/CuO as immobilized membrane-shaped photocatalysts with enhanced photocatalytic H_2 production activity. *J Taiwan Inst Chem Eng*. (2023) 149:104998.
80. Han S, Pu YC, Zheng L, Zhang JZ, Fang X. Shell-thickness dependent electron transfer and relaxation in type-II core-shell CdS/TiO_2 structures with optimized photoelectrochemical performance. *J Mater Chem A*. (2015) 3:22627–35.
81. Chen H, Xie Y, Sun X, Lv M, Wu F, Zhang L, et al. Efficient charge separation based on type-II g-C_3N_4/TiO_2-B nanowire/tube heterostructure photocatalysts. *Dalton Trans*. (2015) 44:13030–9.
82. Liu S, Li Y, Zhong X, Yang K, Li X, Jin W, et al. Metal sulfide-based nanoarchitectures for energetic and environmental applications. *Small Struct*. (2024) 5:2300536.
83. Li H, Zhang J, Li L, Wang H, Jin Z. CdS/$ZnMoS_4$ type II heterojunction interface for enhanced electron transfer and efficient photocatalytic hydrogen production. *J Alloys Compd*. (2025) 1042:184118.
84. Wang Y, Gudino L, Bedia J, Belver C. Solar photocatalytic hydrogen production through metal sulfide/UiO-66-NH_2 heterojunctions. *Sep Purif Technol*. (2025) 353:128663.
85. Low J, Yu J, Jaroniec M, Wageh S, Al-Ghamdi AA. Heterojunction photocatalysts. *Adv Mater*. (2017) 29:1601694.
86. Xu Q, Zhang L, Yu J, Wageh S, Al-Ghamdi AA, Jaroniec M. Direct Z-scheme photocatalysts: principles, synthesis, and applications. *Mater Today*. (2018) 21:1042–63.
87. Huang D, Chen S, Zeng G, Gong X, Zhou C, Cheng M, et al. Artificial Z-scheme photocatalytic system: what have been done and where to go? *Coord Chem Rev*. (2019) 385:44–80.
88. Lu Z, Gao J, Rao S, Jin C, Jiang H, Shen J, et al. A multifunctional membrane based on TiO_2/PCN-224 heterojunction with synergistic photocatalytic-photothermal activity under visible-light irradiation. *Appl Catal B Environ*. (2024) 342:123374.
89. Low J, Jiang C, Cheng B, Wageh S, Al-Ghamdi AA, Yu J. A review of direct Z-scheme photocatalysts. *Small Methods*. (2017) 1:1700080.
90. Li X, Garlisi C, Guan Q, Anwer S, Al-Ali K, Palmisano G, et al. A review of material aspects in developing direct Z-scheme photocatalysts. *Mater Today*. (2021) 47:75–107.
91. Fu Y, Ren Z, Wu J, Li Y, Liu W, Li P, et al. Direct Z-scheme heterojunction of ZnO/MoS_2 nanoarrays realized by flowing-induced piezoelectric field for enhanced sunlight photocatalytic performances. *Appl Catal B Environ*. (2021) 285:119785.
92. Hao X, Cui Z, Zhou J, Wang Y, Hu Y, Wang Y, et al. Architecture of high efficient zinc vacancy mediated Z-scheme photocatalyst from metal-organic frameworks. *Nano Energy*. (2018) 52:105–16.
93. Ouyang C, Quan X, Zhang C, Pan Y, Li X, Hong Z, et al. Direct Z-scheme $ZnIn_2S_4$@MoO_3 heterojunction for efficient photodegradation of tetracycline hydrochloride under visible light irradiation. *Chem Eng J*. (2021) 424:130510.
94. Hu HY, Xie LJ, He L, Wu PP, Lu KQ, Yang K, et al. Constructing metal sulfide-based S-scheme heterojunctions for efficient photocatalytic reaction: a mini review of recent advances. *Curr Opin Chem Eng*. (2024) 44:101021.
95. Lv JR, Guo RT, Zhu HW, Shi XD, Liu MY, Pan WG. Recent advances in metal halide perovskites for CO_2 photocatalytic reduction: an overview and future prospects. *Small*. (2025) 21:2408921.
96. Wang C, Zhao Y, Cheng C, Li Q, Guo C, Hu Y. S-scheme heterojunction photocatalysts: mechanism, challenges and opportunities. *Coord Chem Rev*. (2024) 521:216177.
97. Li J, Yan S, Wu J, Cheng Q, Wang K. Improving hydrogen peroxide photosynthesis over inorganic/organic S-scheme photocatalyst with $LiFePO_4$. *Acta Phys Chim Sin*. (2025) 41:100104.
98. Cheng Q, Li J, Huang Y, Liu X, Zhou B, Xiong Q, et al. Verifying the unique charge migration pathway in polymeric homojunctions for artificial photosynthesis of hydrogen peroxide. *Adv Sci (Weinh)*. (2025) 12:2500218.
99. Qin H, Huang Y, Cheng Q, Yan S, Wang K. Boosting charge transfer at inorganic/organic S-scheme interface for photo-Fenton degradation of antibiotics and bacterial inactivation. *Chin J Catal*. (2025) 72:106–17.
100. Zhou Q, Zhang L, Zhang L, Jiang B, Sun Y. In-situ constructed 2D/2D $ZnIn_2S_4$/$Bi_4Ti_3O_{12}$ S-scheme heterojunction for degradation of tetracycline: performance and mechanism insights. *J Hazard Mater*. (2022) 438:129438.
101. Su Y, Xu X, Li R, Luo X, Yao H, Fang S, et al. Design and fabrication of a CdS QDs/Bi_2WO_6 monolayer S-scheme heterojunction configuration for highly efficient photocatalytic degradation of trace ethylene in air. *Chem Eng J*. (2022) 429:132241.
102. Thakur N, Panwar A, Soni V, Raizada P, Singh P, Khan AAP, et al. Next-generation wastewater treatment with emerging 2D MOF-derived photocatalysts. *ACS Omega*. (2025) 10:58029–56.
103. Dharamalingam K, Kumar BA, Ramalingam G, Florence SS, Raju K, Kumar PS, et al. The role of sodium dodecyl sulfate mediated hydrothermal synthesis of MoS_2 nanosheets for photocatalytic dye degradation and dye-sensitized solar cell application. *Chemosphere*. (2022) 294:133725.
104. Smrithi S, Kottam N, Narula A, Madhu G, Mohammed R, Agilan R. Carbon dots decorated cadmium sulphide heterojunction-nanospheres for the enhanced visible light driven photocatalytic dye degradation and hydrogen generation. *J Colloid Interface Sci*. (2022) 627:956–68.

105. Liu TH, Li Q, Yin HY, Cai XB, Wang ZG, Wu ZQ, et al. Tuning band structures at metal sulfides/Zr-MOF heterojunctions: modulate optical-electronic properties to boost photocatalytic detoxification of Cr(VI) and degradation of reactive dyes. *J Mol Struct*. (2024) 1298:137081.
106. Riaz I, Siddique AB, Mazhar MT, Abuelizz HA, Ali A, Khan I, et al. Tuning the optical and photocatalytic performance of CuO-CdS nanocomposites through Zn doping for wastewater remediation. *Opt Mater*. (2026) 179:118322.
107. Soni V, Singh P, Gautam P, Khan AAP, Dinh DA, Nguyen VH, et al. Novel $ZnTiO_3$-based photocatalysts: nanostructured catalyst design, mechanisms, and applications toward efficient solar-fuel and pollutants degradation. *Ceram Int*. (2026) (in press).
108. Che H, Che G, Jiang E, Liu C, Dong H, Li C. A novel Z-scheme CdS/Bi_3O_4Cl heterostructure for photocatalytic degradation of antibiotics: mineralization activity, degradation pathways and mechanism insight. *J Taiwan Inst Chem Eng*. (2018) 91:224–34.
109. Liu T, Wang B, Wang T, Li C, Wang W, Wang M, et al. One-pot synthesis of Zn-CdS@C nanoarchitecture with improved photocatalytic performance toward antibiotic degradation. *Chemosphere*. (2022) 300:134621.
110. Das C, Shafi T, Thulluru LP, Naushad M, Dubey BK, Chowdhury S. Three-dimensional highly porous MoS_2/graphene aerogel for visible-light-driven photocatalytic degradation of tetracycline. *ACS ES T Water*. (2024) 4:2144–58.
111. Muthuganesh A, Rafi SM, Siddhardhan E, Surender S, Raji RK, Soundranayagam J, et al. Rod-on-sheet g-C_3N_4/CdS hybrid nanostructure for enhanced photocatalytic detoxification of industrial effluents. *Mater Sci Semicond Process*. (2026) 202:110102.
112. Dileepkumar V, Surya P, Pratapkumar C, Viswanatha R, Ravikumar C, Kumar MA, et al. $NaFeS_2$ as a new photocatalytic material for the degradation of industrial dyes. *J Environ Chem Eng*. (2020) 8:104005.
113. Farhan A, Zahid M, Tahir N, Mansha A, Yaseen M, Mustafa G, et al. Investigation of boron-doped graphene oxide anchored with copper sulphide flowers as visible light active photocatalyst for methylene blue degradation. *Sci Rep*. (2023) 13:9497.
114. Xu G, Du M, Li T, Guan Y, Guo C. Facile synthesis of magnetically retrievable Fe_3O_4/$BiVO_4$/CdS heterojunction composite for enhanced photocatalytic degradation of tetracycline under visible light. *Sep Purif Technol*. (2021) 275:119157.
115. Zhou Y, Liu K, Zhuang S, Mu Y. GO/CdS heterojunctions for accelerated photocatalytic antibiotic degradation. *Nanomaterials (Basel)*. (2025) 15:1475.
116. Zhang S, Zhu P, Duan M, He B, Li X, Xin X. Preparation of direct Z-scheme La-doped Bi_2WO_6/CdS with enhanced visible light absorption and its photocatalytic degradation of antibiotics. *Sep Purif Technol*. (2024) 338:126524.
117. Zheng Y, Luo S, Huang H, Tang Y, He J, Yu H, et al. Regulating the surface-interface structure of CdS by inexpensive co-catalyst CoS_2: promoting photocatalytic degradation of antibiotics. *J Environ Chem Eng*. (2025) 13:117675.
118. Lu C, Wang Y, Yang Z, Wang Z, Jiao D, Gong X, et al. Synergistic charge transfer in CdS/MOF S-scheme heterojunction boosts photo-Fenton reaction degradation of tetracycline hydrochloride. *J Environ Chem Eng*. (2025) 13:118902.
119. Luo Z, Leo C, Guo F, Zhao XY. Visible light initiated norfloxacin degradation through a double Z-scheme Bi_2WO_6/ZnO/CdS photocatalyst. *Sep Purif Technol*. (2025) 366:132670.